

## Daily High-Resolution-Blended Analyses for Sea Surface Temperature

RICHARD W. REYNOLDS,\* THOMAS M. SMITH,<sup>+</sup> CHUNYING LIU,\* DUDLEY B. CHELTON,<sup>#</sup>  
KENNETH S. CASEY,<sup>@</sup> AND MICHAEL G. SCHLAX<sup>#</sup>

*\*NOAA/National Climatic Data Center, Asheville, North Carolina*

*+NOAA/NESDIS, CICS/ESSIC, University of Maryland, College Park, College Park, Maryland*

*#College of Oceanic and Atmospheric Sciences, and Cooperative Institute for Oceanographic Satellite Studies,  
Oregon State University, Corvallis, Oregon*

*@NOAA/National Oceanographic Data Center, Silver Spring, Maryland*

(Manuscript received 18 December 2006, in final form 12 April 2007)

### ABSTRACT

Two new high-resolution sea surface temperature (SST) analysis products have been developed using optimum interpolation (OI). The analyses have a spatial grid resolution of  $0.25^\circ$  and a temporal resolution of 1 day. One product uses the Advanced Very High Resolution Radiometer (AVHRR) infrared satellite SST data. The other uses AVHRR and Advanced Microwave Scanning Radiometer (AMSR) on the NASA Earth Observing System satellite SST data. Both products also use in situ data from ships and buoys and include a large-scale adjustment of satellite biases with respect to the in situ data. Because of AMSR's near-all-weather coverage, there is an increase in OI signal variance when AMSR is added to AVHRR. Thus, two products are needed to avoid an analysis variance jump when AMSR became available in June 2002. For both products, the results show improved spatial and temporal resolution compared to previous weekly  $1^\circ$  OI analyses.

The AVHRR-only product uses Pathfinder AVHRR data (currently available from January 1985 to December 2005) and operational AVHRR data for 2006 onward. Pathfinder AVHRR was chosen over operational AVHRR, when available, because Pathfinder agrees better with the in situ data. The AMSR–AVHRR product begins with the start of AMSR data in June 2002. In this product, the primary AVHRR contribution is in regions near land where AMSR is not available. However, in cloud-free regions, use of both infrared and microwave instruments can reduce systematic biases because their error characteristics are independent.

### 1. Introduction

Sea surface temperature (SST) is an important variable to better understand interactions between the ocean and the atmosphere. SST analyses convert irregularly spaced SST data to a regular grid and have been used for many purposes from climate monitoring and prediction (e.g., Smith and Reynolds 2003) to feature tracking (e.g., Quartly and Srokosz 2002). Often the planned purpose for the analysis strongly influences the analysis resolution and accuracy. Thus, for example, a SST analysis designed for climate research may have reduced spatial and temporal resolution in order to reduce sampling errors. This can occur (as discussed be-

low) in the western boundary current regions in winter where clouds can reduce high-resolution infrared (IR) satellite sampling while lower-resolution microwave satellite data is not impacted.

In this paper the focus is on improving the resolution of the climate-scale SST analyses produced at the National Oceanic and Atmospheric Administration (NOAA) as described by Reynolds and Smith (1994) and Reynolds et al. (2002). These older analyses use IR satellite data from the Advanced Very High Resolution Radiometer (AVHRR) and in situ data from ships and buoys. The analyses are performed weekly on a  $1^\circ$  spatial grid from November 1981 to present by optimum interpolation (OI) with a separate step to correct any large-scale satellite biases relative to the in situ data. The Reynolds and Smith (1994) and Reynolds et al. (2002) weekly OI will henceforth be referred to as OI version 1 (OI.v1) and OI version 2 (OI.v2), respectively. The techniques for these analyses were originally

---

*Corresponding author address:* Richard W. Reynolds, NOAA/National Climatic Data Center, 151 Patton Ave., Asheville, NC 28801-5001.

E-mail: Richard.W.Reynolds@noaa.gov

designed in the late 1980s and early 1990s when there was only one AVHRR satellite instrument producing SSTs. Thus, the spatial scales of the OI were designed conservatively.

Since the late 1990s, more satellite datasets have become available and there have been frequent comparisons of other data and analyses with the OI.v2. These results have strongly suggested that spatial and temporal improvements were needed. Perhaps the most convincing study was the work of Chelton and Wentz (2005), hereafter CW05, which focused on six regions in the World Ocean with strong SST fronts. In these comparisons, data from the Advanced Microwave Scanning Radiometer (AMSR) on the NASA Earth Observing System satellite were used. AMSR is the first microwave (MW) sensor that can retrieve SSTs from a satellite with global coverage. The data record begins in June 2002. CW05 also used AVHRR data from the version 5 Pathfinder reanalysis project in the comparison and two analyses: the OI.v2 and the National Centers for Environmental Prediction (NCEP) daily Real Time Global SST (RTG\_SST) analysis (Thiébaux et al. 2003). The RTG\_SST analysis is based on the same data used in the OI.v2. However, the RTG\_SST has been produced daily since 30 January 2001 on a  $1/2^\circ$  grid, and it uses smaller spatial error correlation scales than those used in the OI.v2. (A higher resolution  $1/12^\circ$  daily analysis was implemented on 27 September 2005.) CW05 showed that the gradients in RTG\_SST analysis agreed better with AMSR than the OI.v2. Because the RTG\_SST and OI.v2 use AVHRR and in situ data that are independent of AMSR, this is strong evidence that the OI.v2 analysis can be improved even in the 1980s when only AVHRR data were available.

The objective of this study is to refine the OI.v2 analysis procedure to produce a higher-resolution reanalysis product dating back to January 1985 and maintained operationally in real time. The analysis will be designed to better resolve features such as the strong fronts described in CW05. This analysis will be more useful for hurricane forecasting, fisheries (through better location of isotherms and the fish that follow them), and as a boundary condition for atmospheric models. In particular the impact of AVHRR and AMSR SST data will be assessed.

The new analysis that will be developed here is based on OI. This is partly because of the success of the OI.v2. However, there are many similar methods. For example Thiébaux et al. (2003) uses a variational method that iterates a solution based on steepest descent. Reynolds et al. (2002) investigated this method and found the resulting solution to be almost identical to the OI. The variational method was computationally more efficient.

However, it required some constraints of the error statistics that were not required for the OI. Kriging is another technique that is equivalent to the OI, as discussed by Hock and Jensen (1999). They mention that kriging and OI were developed for geology and meteorology, respectively, and that the initial papers on the analysis methods were first published in 1963.

As discussed in CW05, clouds are essentially transparent to MW radiation and AMSR SSTs can be obtained in all conditions free of precipitation. Infrared measurements can only be obtained in clear-sky conditions, and cloud-contaminated data are often difficult to identify (e.g., Cayula and Cornillon 1996; Stowe et al. 1999). As shown by CW05, combined daytime and nighttime MW coverage in 3-day averages is greater than 95% over most of the World Ocean while IR coverage is less than 25% in cloudy regions. Because of the resolution and sampling limitations of MW and IR measurements of SST, a  $0.25^\circ$  latitude/longitude grid was selected. This choice will simplify comparisons of analysis products using IR and MW satellite products.

The temporal resolution for the analysis was selected to be daily. This selection ignores the diurnal cycle, which cannot be properly resolved using only one polar orbiting instrument. Furthermore, as discussed in section 3 all satellite data are bias adjusted relative to 7 days of in situ data, which further reduces any diurnal signal. Thus, the OI analysis is a daily average SST that is bias adjusted using a spatially smoothed 7-day in situ SST average.

Potential users of satellite data should be aware that there are now many additional data products and analyses that are operational or under development (Donlon et al. 2002). Many of these are part of the Global Ocean Data Assimilation Experiment (GODAE) high-resolution sea surface temperature pilot project (GHRSSST, more information available online at <http://www.ghrsstpp.org/>, see in particular "Data Access"). These include estimates of the diurnal cycle and analyses using both geostationary and polar orbiting satellite data. The analyses are computed over a variety of regions and time periods with different spatial and temporal resolutions. Users have a choice of analyses that was never possible before GHRSSST was established.

Many analyses use as many data input files as possible to obtain the most accurate product at a given time (Kawai et al. 2006). However, this choice may lead to abrupt jumps in the resolution of the analyses at times when new satellite instruments become available or old instruments are terminated. This nonstationarity of the mapping error complicates the accuracy and resolution of the SST for climate variability. To avoid this, each satellite product should be compared sepa-

rately before combining them. This is most important when data are obtained from satellites in very different orbits such as geostationary versus polar, or from instruments with very different resolution and sampling such as IR and MW.

Anomalies in this paper are computed relative to the Xue et al. (2003) monthly climatology, which has a base period of 1971–2000 and a spatial resolution of  $1^\circ$ . The finer spatial and temporal resolution required for the daily OI is computed by linear interpolation.

In the sections that follow, the data used in this version of the daily OI will first be discussed. This is followed by a short discussion of the OI analysis procedure with error statistics appropriate for the daily OI analysis. A new satellite bias correction method is then discussed along with a more complete analysis error estimate that includes sampling, random, and bias errors. This discussion is followed by detailed analysis intercomparisons showing progress and problems. The analyses used in the comparison will be limited to the analyses presented here and those presented in CW05. The paper ends with a summary of conclusions and future plans.

## 2. Data

The two new daily OI SST products presented in this study use satellite SST retrievals, SST observations from ships and buoys, and proxy SSTs generated from sea ice concentrations. Each of these data sources is summarized in this section.

### *a. Satellite SST retrievals*

At this time there are a number of different polar and geostationary satellites that produce SST retrievals. For the daily OI, AVHRR and AMSR instruments were selected as the initial set of satellite instruments. They represent the longest global record of IR and MW retrievals.

As described by CW05, AMSR SST retrievals are made along with several other variables including wind speed and precipitation. The AMSR SST retrievals have a footprint size of 56 km and are contaminated within about 75 km of land or ice and during precipitation events. The primary advantage of AMSR data is the near-all-weather measurement capability. Except in the intertropical convergence zone (ITCZ) where precipitation is persistent, only a few percent of MW SSTs are lost due to precipitation contamination. AMSR data, version 5, are obtained from Remote Sensing Systems as twice daily gridded averages on a  $0.25^\circ$  grid (more information available online at [http://www.ssmi.com/amr/amr\\_browse.html](http://www.ssmi.com/amr/amr_browse.html)).

In the OI.v1 and OI.v2 analyses, an operational AVHRR product was used. Details on the algorithm can be found in May et al. (1998); only a brief sketch is presented here. The biggest challenge in retrieving SST from an IR instrument is the previously mentioned cloud detection problem. Once clouds have been eliminated, the SST retrieval algorithm is designed to minimize the effects of atmospheric water vapor using two or three IR channels. The SST algorithms are “tuned” using regression of SST against quality-controlled buoy data. This procedure converts the retrieval of the temperature of the “skin” (roughly a micron in depth) to a “bulk” (roughly 0.5 m in depth) SST. To make this procedure as stable as possible, the tuning procedure is done globally with several weeks of data. In this procedure it is important that the SST range of the buoy and satellite data be roughly similar. If, for example, buoy SSTs were not available above  $20^\circ\text{C}$ , then tuned satellite retrievals above  $20^\circ\text{C}$  would not be properly corrected (Emery et al. 2001). Furthermore, if the satellite SST retrievals are partially contaminated by clouds, they have a negative bias because cloud temperatures are nearly always colder than the SSTs. Negative biases can also be caused by atmospheric aerosols, especially stratospheric aerosols from large volcanic eruptions (see Reynolds et al. 1989; Reynolds 1993). In addition, biases of either sign can be due to other problems including instrument design and instrument aging.

AVHRR instruments with multichannel capabilities have been available on NOAA polar orbiters since November 1981. However, the data from the Pathfinder AVHRR reanalysis project begins in January 1985.<sup>1</sup> The Pathfinder version 5 AVHRR data are based on one satellite instrument with twice-daily gridded averages on a 4.6-km grid (more information available online at <http://pathfinder.nodc.noaa.gov>). These data are produced by the University of Miami and the NOAA/National Oceanographic Data Center, and represent an improvement over the previously available Pathfinder version 4 AVHRR data (Kilpatrick et al. 2001). Pathfinder data have the potential of being better than the operational product because a reanalysis allows corrections to the AVHRR dataset in a delayed mode. Thus, for example, correction of the operational satellite retrievals following a volcanic eruption would be delayed by the response time to modify the algorithm.

---

<sup>1</sup> Five-channel AVHRR NOAA-7 data began in November 1981 and ended in January 1985. Pathfinder did not process NOAA-7 data because buoy data, which are used to tune the algorithm, were sparse during this time period. Experiments are being conducted now, however, to extend the Pathfinder time series to include these early years.

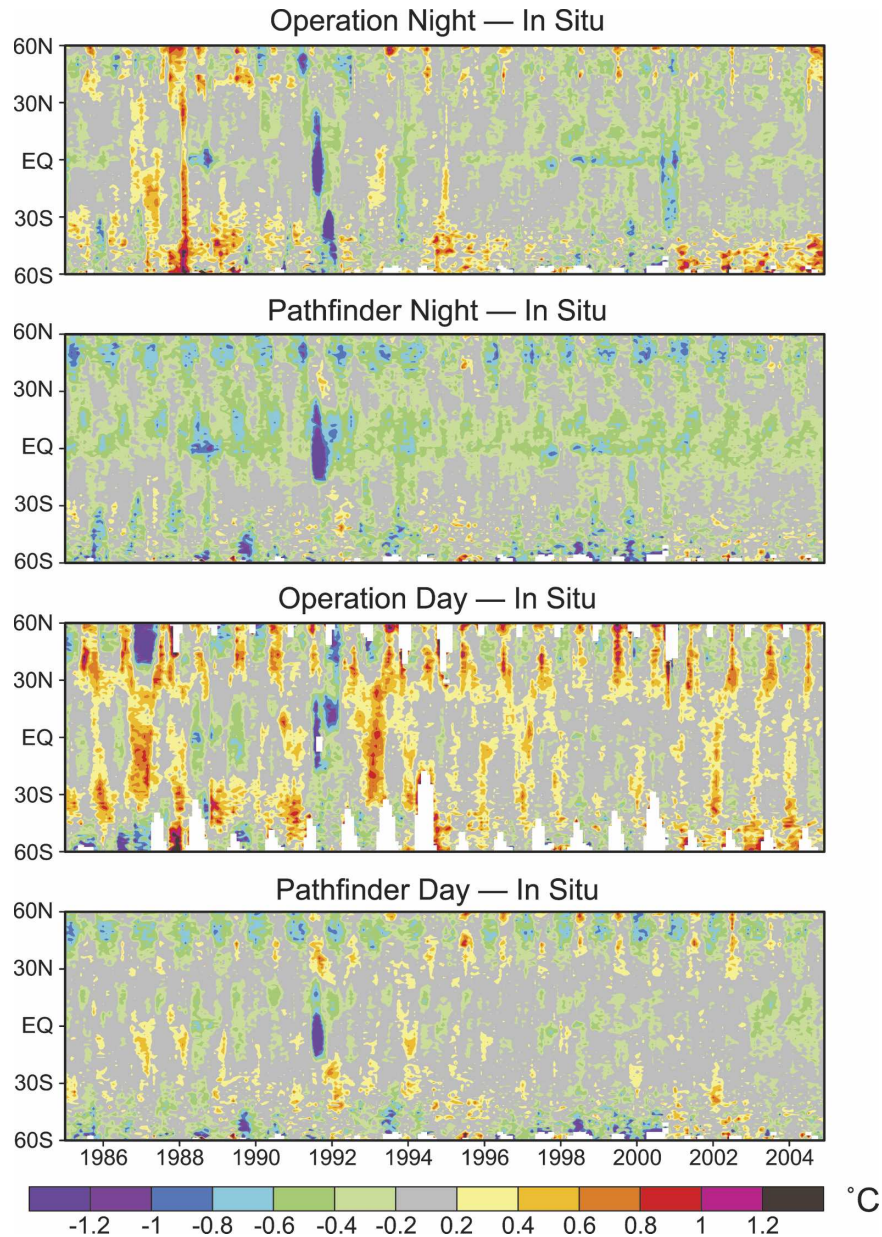


FIG. 1. Zonal-averaged differences of AVHRR data products minus in situ data. (top to bottom) The AVHRR data products are operational night, Pathfinder night, operational day, and Pathfinder day. Zonal monthly averaged satellite and in situ data anomalies are generated on a  $1^\circ$  latitude grid and then differenced. Pathfinder AVHRR was selected for the OI.

To examine differences between Pathfinder and operational SST retrievals, the zonal monthly averages of the satellite minus in situ SST anomaly differences were computed on a  $1^\circ$  latitude grid for both AVHRR Pathfinder and AVHRR operational products. (Details on the in situ data follow in section 2b.) Figure 1 shows the nighttime and daytime satellite differences with respect to all in situ data (day and night combined). The same in situ reference is used in all panels. Pathfinder

nighttime and daytime differences are less variable over time than the corresponding operational daytime and nighttime differences. There are also clear seasonal cycles in the northern midlatitudes where the daytime operational product is warmer than the in situ data in summer and both the nighttime and daytime Pathfinder products are cooler in winter. There are some other large operational differences near the beginning of 1988 and 2001 that may be due to instrumental problems that

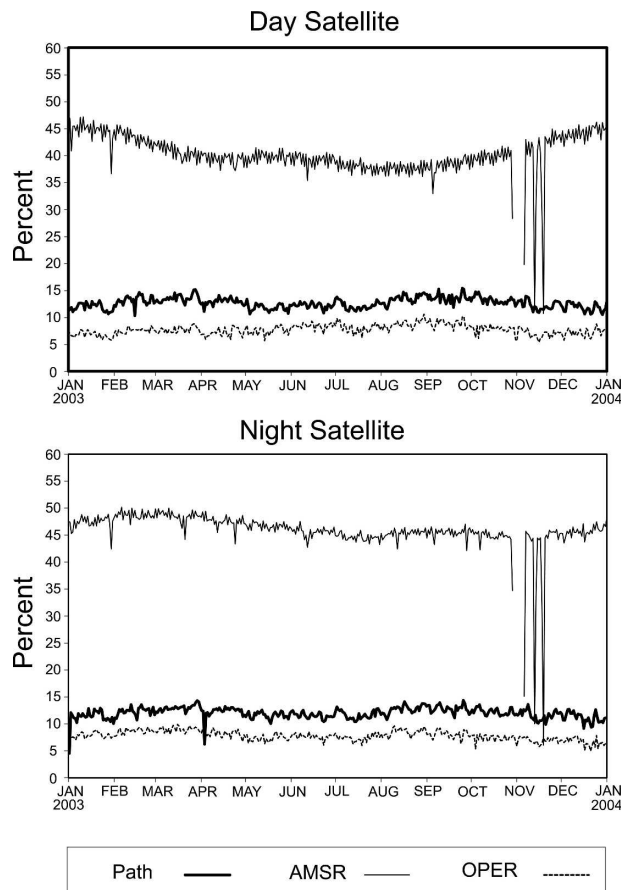


FIG. 2. Daily percentage of  $\frac{1}{4}^\circ$  ocean grid boxes with day and nighttime satellite data. The types of data are Pathfinder AVHRR, operational AVHRR, and AMSR. The maximum number of ocean boxes is 691 454. The AMSR data were completely missing from 30 Oct to 5 Nov 2003.

occurred near the end of the lifetimes of the *NOAA-9* and *NOAA-14* instruments, respectively. In addition, negative biases related to Mt. Pinatubo (1991–92) are less extensive in the Pathfinder differences. Unfortunately, Pathfinder does have a nighttime residual negative bias, especially in the Tropics. A spatial map of the differences (as will be shown later) indicates that these differences occur over regions that are generally cloudy [e.g., the ITCZ and the South Pacific convergence zone (SPCZ)]. These differences occur even though only Pathfinder data with the lowest errors (quality control flag 7) were used.

It is useful to also examine the data coverage of AMSR and the two AVHRR versions. Figure 2 shows the percentage of daily oceanic  $\frac{1}{4}^\circ$  grid boxes that have either daytime or nighttime observations for 2003. The results for AVHRR use the same satellite instrument. For the AVHRR, the results show that the average day and night operational AVHRR coverage is 8%, while

the day and night Pathfinder coverage is 13% and 12%, respectively. (If day and night are combined, the operational and Pathfinder AVHRR coverage increases to 16% and 25%, respectively.) Because this is the same sensor, the different coverage is evidently due to different cloud masking. The tropical negative biases in Pathfinder SSTs (Fig. 1) may therefore be an indication of cloud detection errors. Because the overall Pathfinder AVHRR minus in situ month-to-month variability is lower than the operational AVHRR minus in situ variability, Pathfinder will be used in the daily OI when available. As Pathfinder processing is not done in real time, the operational AVHRR product will be used for the most recent data period (presently beginning 1 January 2006). This is not an ideal solution. However, the bias correction, as discussed in the next section, will take care of most large-scale biases on temporal scales of 7 days or longer. During the operational AVHRR record, biases occurred as satellite instruments failed or as the atmosphere changed (e.g., due to addition of volcanic aerosols). Thus, the reanalysis of Pathfinder AVHRR is a better choice. In addition, the bias correction with respect to the in situ data (discussed in section 3b) eliminates any transition between Pathfinder and operational AVHRR except south of  $40^\circ$ – $50^\circ$ S where in situ data are sparse. The potential bias error south of  $40^\circ$ – $50^\circ$ S is defined in section 3b and demonstrated through analysis intercomparisons in section 4. Note that the ocean grid boxes include coastal regions, the Great Lakes, and the Caspian Sea, as well as Arctic and Antarctic regions that may be covered by sea ice. If ocean regions poleward of  $70^\circ$  latitude are excluded, the percentages given above and shown in Fig. 2 increase by a factor of 1.2.

AMSR coverage has a clear advantage over AVHRR (Fig. 2), as expected. AMSR raises the daily coverage for day and night to 40% and 46%, respectively. (If day and night are combined, the average AMSR coverage increases to 86%.) Note that the daytime AMSR has a gradual decrease in observations from April through August. This occurs every year due to contamination of measurements by daytime sun glint between  $50^\circ$  and  $10^\circ$ S (C. Gentemann 2006, personal communication). Also there are periods where AMSR data are missing. The largest one occurred between 30 October and 5 November 2003 due to a spacecraft problem during which none of the onboard sensors were operational. This reduction of data results in a noticeable drop in the daily OI gradient, which will be discussed later.

For the analyses in section 4, daytime AVHRR, nighttime AVHRR, daytime AMSR, and nighttime AMSR were separately averaged onto a  $\frac{1}{4}^\circ$  grid. Separate analyses will be produced using AVHRR alone,

AMSR alone, and AVHRR and AMSR combined. All analyses use in situ data and proxy estimates of SSTs obtained from sea ice as discussed below.

### b. In situ data

The in situ SST data are from observations from ships and buoys (both moored and drifting) obtained from the International Comprehensive Ocean–Atmosphere Dataset (ICOADS; e.g., Worley et al. 2005). Most ship observations in the 1985–2006 period were made from insulated buckets, hull contact sensors, and engine condenser intakes at depths of one to several meters. Although selected SST observations can be very accurate (see Kent et al. 1999; Kent and Taylor 2006), typical rms errors of individual observations from ships are larger than 1°C and may have biases of a few tenths of a degree Celsius. SST observations from drifting and moored buoys are typically made by a thermistor or hull contact sensor and usually are obtained in real time by satellites. Although the accuracy of the buoy SST observations varies, the random error is usually smaller than 0.5°C, which is significantly smaller than ship SST errors.

### c. Sea ice to SST conversion algorithms

In situ and satellite observations tend to be sparse in the marginal ice zone (MIZ). Thus, as was done in the OI.v2, sea ice data were used to obtain proxy estimates of SST. Operationally the OI.v2 uses real-time sea ice concentrations generated from microwave satellite data by Grumbine (1996) with delayed sea ice concentrations by Cavalieri et al. (1999). The Grumbine product has been gathered from different sources and has not been reanalyzed to produce a consistent long-term dataset. This problem can be clearly seen in Fig. 3, which compares Northern and Southern Hemisphere coverage for the two sets of sea ice data. In particular, the Southern Hemisphere shows a seasonal amplitude change after 1991 with several temporary jumps in 1995–96. [R. W. Grumbine (2006, personal communication) is planning to correct this]. For the daily OI presented in this study, the Cavalieri sea ice is used through December 2004 and the Grumbine sea ice is used after 2004. Use of one consistent product available in real time would be preferable to avoid potential inconsistencies between products such as the difference in the Northern Hemisphere winter maxima (Fig. 3). At this time, however, a consistent real-time, long-term set does not exist.

In the OI.v2 based on Rayner et al. (2003) a quadratic relationship was defined between sea ice concentration and SST:

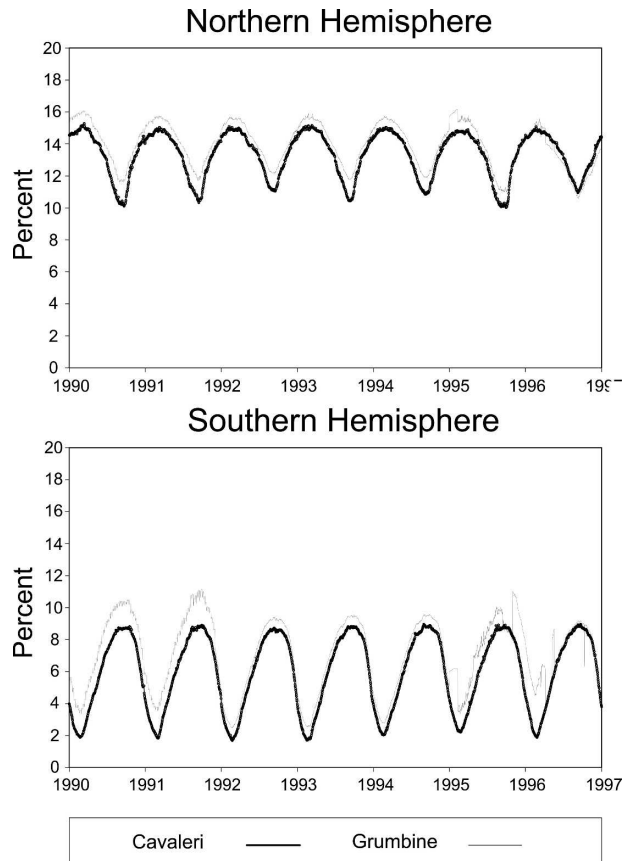


FIG. 3. Daily percentage of  $\frac{1}{4}^\circ$  ocean grid boxes with sea ice coverage from two products: Cavalieri et al. (1999) and Grumbine (1996). The period is 1 Jan 1990–1 Jan 1997. Note the irregularities in the Grumbine dataset.

$$T_I = aI^2 + bI + cI \geq I_0, \quad (1)$$

where  $T_I$  is the simulated SST,  $I$  is the ice concentration fraction, which varies from 0 (0%) to 1 (100%), and  $I_0$  is the minimum value of  $I$  used to simulate SSTs. The coefficients are assumed to be locally constant by month and by region. A simpler linear version

$$T_I = b'I + c', \quad I \geq I_0 \quad (2)$$

is also considered here. The coefficients  $a$ ,  $b$ ,  $c$ ,  $b'$ , and  $c'$  in the empirical relationships (1) and (2) are determined by regression for  $30^\circ$  wide longitude bands (or sectors) for the Northern and Southern Hemispheres. For both equations the coefficients are constrained so that  $T_I$  is equal to the freezing point of water ( $-1.8^\circ\text{C}$  for seawater and  $0^\circ\text{C}$  for freshwater) for ice concentrations of  $I = 1$ .

In appendix A, (1) and (2) are evaluated. The procedure is carried out by determining the coefficients for a 10-yr dependent period and then evaluating the rms and bias differences between the simulated and actual

SSTs for a 10-yr independent period. The rms differences increased in both fits with decreasing ice concentration. In addition, the absolute biases were typically smaller for the linear fit for ice concentrations  $>0.5$  and smaller for the quadratic fit for ice concentrations  $<0.5$ . For some quadratic fits (not shown) data were sparse and the quadratic fit occasionally generated SSTs that were unstable at low sea ice concentrations. As a conservative approach,  $I_o$  was set to 0.5 and the linear fit (2) was selected over the quadratic fit. This selection avoided the problem of the unstable quadratic fit. It seemed better to let the OI fill in the values between the actual SST data and the simulated sea ice for  $I < 0.5$ , rather than simulating SSTs where rms differences were large. Thus, SSTs were simulated from ice concentrations for  $I \geq 0.5$  using (2): no SSTs were simulated for  $I < 0.5$ .

For actual use in the daily OI, the coefficients were recomputed for the entire 20-yr period (1985–2004). The sea ice data indicated the presence of summer sea ice in the Great Lakes in 2003. This resulted in sea-ice-simulated SSTs that led to  $-18^\circ\text{C}$  anomalies in Lake Ontario. The sea ice algorithms were not designed for low salinity water (D. J. Cavalieri 2006, personal communication). Simulated SSTs for sea ice were therefore not used in the Baltic nor in the Great Lakes. (Sea ice concentrations are not produced regularly for the Caspian Sea, so no ice simulated SSTs were generated there.) In addition, occasional 1-day noise events were noted in both the Cavalieri and Grumbine ice fields. During these events, the ice concentrations increased dramatically, especially in coastal regions, resulting in spikes in the daily OI from the sea-ice-simulated SSTs. To eliminate this problem, a 7-day median filter was applied temporally to all daily ice fields, and the simulated SSTs were computed from the median smoothed sea ice data.

### 3. Analysis

The OI.v2 analysis includes a preliminary correction of the AVHRR satellite data with respect to the in situ data before they are used in the OI (Reynolds et al. 2002). This initial step is necessary because the OI method assumes that the data do not contain long-term biases. For comparisons, the daily OI is processed with and without this bias correction. In sections 3a–c, the OI procedure is discussed first, followed by the satellite bias correction procedure.

#### a. The OI analysis

The OI analysis is performed on a regular grid using irregularly spaced data. The analysis is formed by a

weighted sum of the data, using the OI linear weights,  $w_{ik}$ , determined by regression. In this section, the indices  $i$  and  $j$  will be used for data while  $k$  will be used for analysis grid points. The relationship can be expressed (see Reynolds and Smith 1994, for details) as

$$r_k = \sum_{i=1}^N w_{ik} q_i, \quad (3)$$

where  $q_i$  are the SST data values,  $N$  is the number of data values,  $r_k$  is the analyzed SST, and normally  $q$  and  $r$  are differences from a first-guess reference system, which is defined here as the analysis from the previous time step. Thus, in the daily OI,  $q$  and  $r$  are the SST data and analysis increments, defined as the difference from the analysis at the previous time step.

The weights are formally defined following Reynolds and Smith (1994). Here the ensemble average of the analysis correlation error  $\langle \pi_i \pi_j \rangle$  is assumed Gaussian, expressed as

$$\langle \pi_i \pi_j \rangle = \exp \left[ \frac{-(x_i - x_j)^2}{\lambda_x^2} + \frac{-(y_i - y_j)^2}{\lambda_y^2} \right]. \quad (4)$$

The variables  $x$  and  $y$  are the zonal and meridional data and analysis locations, and  $\lambda_x$  and  $\lambda_y$  are the zonal and meridional spatial scales, discussed below. The weights can then be defined (following Reynolds and Smith 1994) by

$$\sum_{i=1}^N (\langle \pi_i \pi_j \rangle + \varepsilon_i^2 \delta_{ij}) w_{ik} = \langle \pi_j \pi_k \rangle, \quad (5)$$

where  $\varepsilon_i$  is the noise-to-signal standard deviation ratio, which also needs to be determined. The ensemble averages of the data errors are assumed uncorrelated between different observations. Thus, the data correlation error is  $\delta_{ij} = 1$  for  $i = j$  and  $\delta_{ij} = 0$ , otherwise.

It is important to note that the actual SSTs (data and analysis) only appear in (3). The remaining equations to determine the weights depend only on the distance via (4) and noise-to-signal ratios for the available SST data. For each analysis grid point,  $\varepsilon_i$ ,  $\lambda_x$ , and  $\lambda_y$  are assumed locally constant and the set of equations are solved to determine the weights and the analyzed SST,  $r_k$ . Spatial functions are defined for each of these quantities with different fields of  $\varepsilon_i$  for each type of data. Presently, the data types are ships, buoys, SST simulated for sea ice, and day and night satellite data for each instrument.

The set of linear equations defined by (5) is solved at each grid point,  $k$ . To reduce computing time, only data points near the analyzed grid point are used. This approach is reasonable because (4) approaches zero with

increasing data-to-gridpoint distance. Furthermore, the solution of the set of linear equations becomes more difficult to solve when data points approach each other because the rows defining  $\langle \pi_i \pi_j \rangle + \varepsilon_i^2 \delta_{ij}$  become closer to each other, leading to a degenerate solution (i.e., the determinant approaches zero). To avoid this possibility, each type of observation within a grid box is averaged into a superobservation for the grid box, which is assumed to be at the center of the box. Next, all superobservations within each box are combined. The combination is carried out using a simplified optimum averaging technique (Kagan 1979) assuming that the local error correlations within each box can be approximated as 1. This method performs an optimal combination of all superobservations values,  $q_i$ , and the super noise-to-signal ratios,  $\varepsilon_i$ , within a grid box into a combined observation and reduced combined noise-to-signal ratio (see appendix B for details). The combined observations and noise-to-signal ratios are the variables actually used in (3)–(5). This method is a two step process, an OA followed by an OI, which approximates an OI-only procedure. However, the two step process is computationally more efficient.

To solve (5), a box centered on each grid point was defined that contains all the observations to be used for that grid point. Recall that the OA method will combine all observations within a grid box,  $0.25^\circ$ . Thus,  $N$  is not only the number of observations;  $N$  is also the number of grid boxes with data. The box size is defined to be  $R_{\max}$  and the maximum number of observations was limited to a specified value of  $N$ ,  $N_{\max}$ . Next, rough weights were computed for the special case where off-diagonal elements in (5) were zero. In that case, the rough weights would be  $w_{jk} = \langle \pi_j \pi_k \rangle / (1 + \varepsilon_j^2)$ . The rough weights were ordered by decreasing magnitude and only data points corresponding to the largest ones were selected such that  $N \leq N_{\max}$ . The algorithm to solve (5) includes a parameter to show when the determinant is close to zero. In that case,  $N_{\max}$  is reduced for that grid point and a reduced set of observations is selected using the ordered rough weights. For the daily OI,  $R_{\max}$  was set to 400 km and  $N_{\max}$  to 22.

It is necessary to determine the spatial correlation scales and noise-to-signal ratios. These scales are specific to the first-guess reference system used to define  $q$  and  $r$  in (3) and here are based on the previous day's OI as first guess. The scales computed for the weekly OI.v1 and OI.v2 could not therefore be used. Following Reynolds and Smith (1994), spatial lagged correlations were computed zonally and meridionally for each grid point. Fitting procedures yield average  $\lambda_x$  and  $\lambda_y$  for AMSR and AVHRR and  $\varepsilon$  for each type of data. For operational AVHRR, the day and night algorithms are

TABLE 1. Noise-to-signal standard deviation ratios and spatial correlation scales as used in the weekly OI.v1 and in the high-resolution daily OI.

Variable	OI.v1	Daily OI
$\varepsilon$ ship	3.90	1.94
$\varepsilon$ buoy	1.50	0.50
$\varepsilon$ ice	1.00	0.50
$\varepsilon$ day AVHRR	1.46	0.50
$\varepsilon$ night AVHRR	0.88	0.50
$\varepsilon$ day AMSR	—	0.35
$\varepsilon$ night AMSR	—	0.35
$\lambda$ zonal	859 km	151 km
$\lambda$ meridional	608 km	155 km

different. However, the day and night algorithms are the same for AMSR and Pathfinder AVHRR. Thus, for each satellite instrument the same values of  $\varepsilon$  were used for both day and night.

The results of these statistical estimates are summarized in Table 1 for the average values ( $60^\circ\text{S}$ – $60^\circ\text{N}$ ) for both the OI.v1 and the new daily OI. (The OI.v2 used values that were slightly modified from those of the OI.v1.) The noise-to-signal ratios are much smaller for the daily OI than the OI.v1. The biggest change occurs in the spatial correlation scales, which are greatly reduced for the daily OI (Fig. 4). In the OI.v2, the average zonal and meridional spatial scales were 850 and 615 km, respectively. Note that the overall zonal and meridional scales in Fig. 4 are similar and could be made isotropic. These scales vary somewhat geographically: they are larger in the Tropics (150–200 km) than at higher latitudes (100–150 km) and smallest (50–100 km) primarily in the regions of western boundary currents. The much smaller correlation scales for the new daily OI compared to those used for the OI.v1 and OI.v2 allow much finer spatial resolution of the SST field.

The choice of the spatial error scales,  $\lambda$ , partially determines the spatial smoothing. If  $\lambda$  is equal to the size of the grid box, then each grid box is analyzed independently. This would make the analysis very noisy because many grid boxes (see Fig. 2) would have no data prior to the availability of AMSR SST data. However, if  $\lambda$  were very large (e.g., 1000 km) many of the finer gradient details would be reduced, as there are in the OI.v2.

To illustrate the impact of  $\lambda$ , the daily OI analysis was produced using the scales in Fig. 4 and using a constant scale of  $\lambda = 50$  km. The analyses were run using AVHRR-only and AMSR and AVHRR combined data. The SST anomalies are shown for 1 July 2003 in Fig. 5. Because the differences are relatively small, the

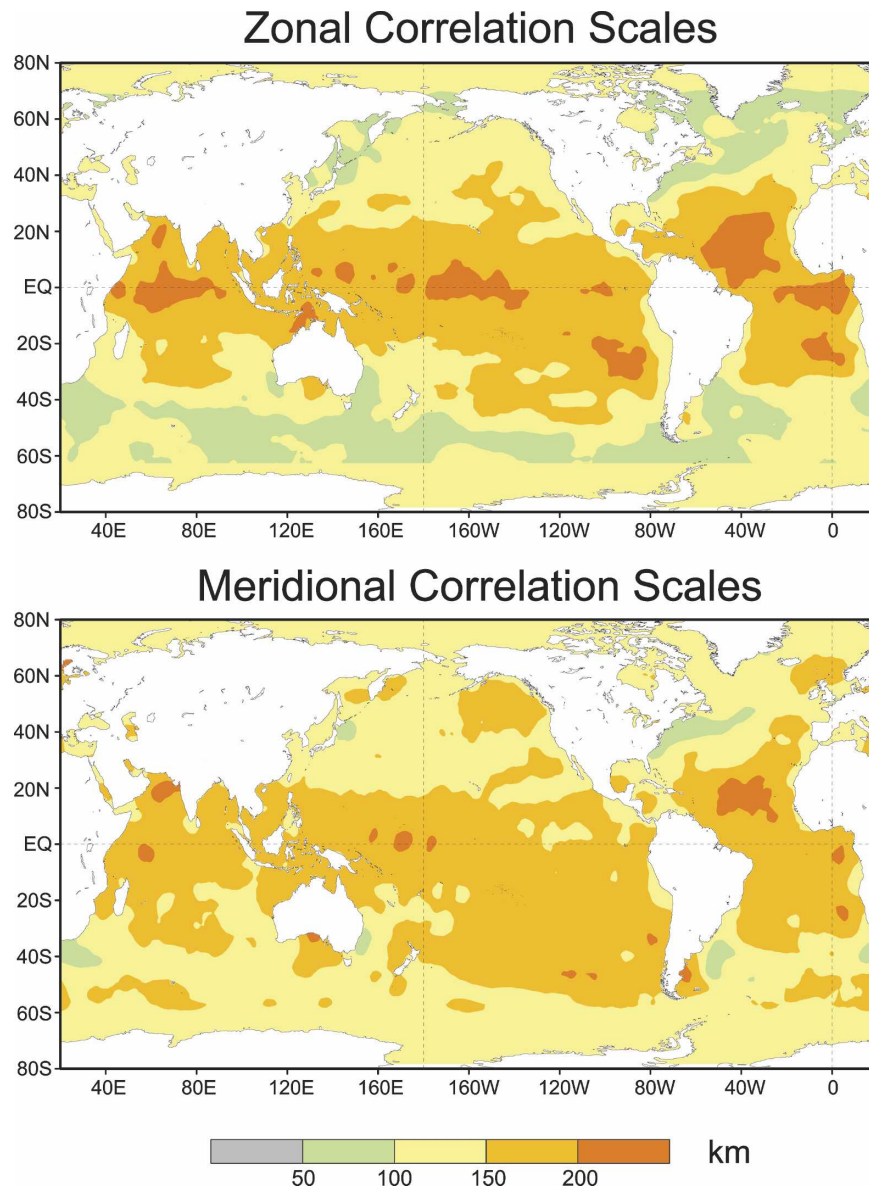


FIG. 4. Zonal and meridional error correlation scales used in the daily OI. The smallest scales are in the western boundary current regions; the largest are in the Tropics. Missing data limited computations south of 60°S and north of 70°N; these values were filled by the southern and northern midlatitude averages, respectively.

anomalies are shown for part of the Southern Hemisphere. This region and date were selected to emphasize the impact of winter clouds on the analyses. The results show that the difference in  $\lambda$  makes almost no difference between the two AMSR and AVHRR analyses. This is because most grid points have AMSR data. Thus, the  $N_{\max}$  limit of 22 grid points is more important than the change in  $\lambda$ . If the two AMSR and AVHRR analyses are now compared with the AVHRR-only analysis with variable  $\lambda$ , the AVHRR-only anomalies appear similar but are a little weaker and smoother

especially in the Falkland Current region near 40°S, 50°W. This weakening of the anomalies is due to the limited AVHRR data compared to AMSR. However, the AVHRR-only anomalies using the constant  $\lambda = 50$  km are reduced even more, especially in the Falkland Current region. In this region AVHRR retrievals tend to be missing due to cloud cover. Here the value of  $\lambda$  is more important than  $N_{\max}$ . In the AVHRR-only analysis with constant  $\lambda$ , the smaller values of  $\lambda$  limit spatial smoothing, which reduces the large-scale impact of AVHRR data.

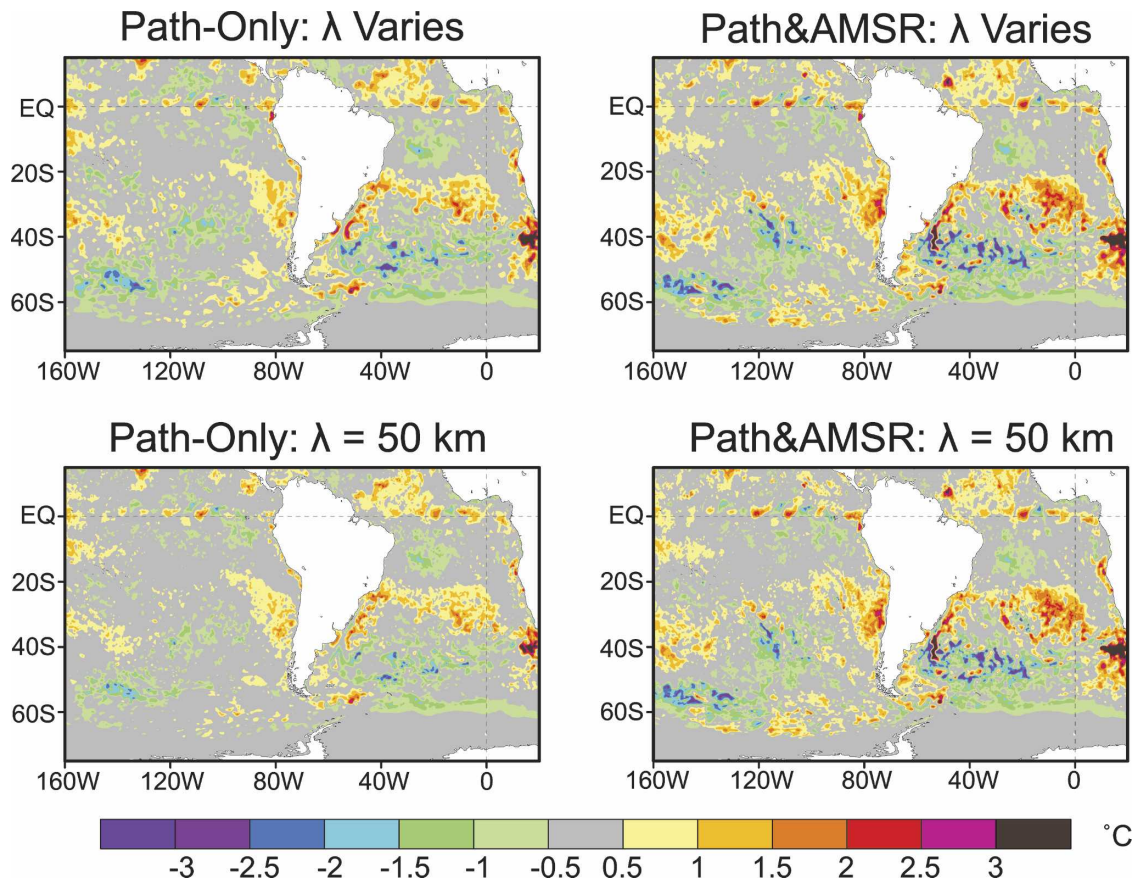


FIG. 5. Daily OI anomalies for 1 Jul 2003. (left) The bias-corrected AVHRR-only daily OI. (right) The bias-corrected AMSR and AVHRR combined daily OI. (top) The variable correlation scales,  $\lambda$ , shown in Fig. 4, and (bottom) a constant correlation scale of  $\lambda = 50$  km.

The final requirement is to determine the OI random and sampling error,  $E_k^2$ . (The bias error will be computed in the bias correction step that follows.) It is determined following Reynolds and Smith (1994) for the OI.v1:

$$E_k^2 = V_k^2 \left( 1 - \sum_{i=1}^N w_{ik} \langle \pi_i \pi_k \rangle \right), \quad (6)$$

where  $V_k^2$  is the AVHRR OI analysis increment variance. [Note that the final subscript in (6) has been corrected; there was a typographical error in the equivalent equation in Reynolds and Smith (1994).] The expected random and sampling error defined by (6) reduces  $V_k^2$  by the observations used in the OI. The standard deviation,  $V_k$ , (see Fig. 6) is largest in western boundary current regions and smallest in the subtropical convergence areas and at high latitudes.

#### b. The bias correction

In the OI.v1 and OI.v2, satellite biases are corrected relative to the in situ data using Poisson's equation

( $\nabla^2 \Phi = \rho$ ), where  $\rho = \nabla^2 \Psi$ ,  $\Psi$  is the initial satellite field, and  $\Phi$  is the corrected satellite field. Here  $\Phi$  is set equal to the value of the in situ field,  $T$ , wherever  $T$  is considered sufficiently accurate. All variables were defined weekly on a  $2^\circ$  spatial grid and  $T$  was defined to be of sufficient accuracy when the number of in situ gridded observations during the week was at least five. This method determined  $\Phi$  at each time step. A problem with this method is that the threshold of five for sufficient accuracy of  $T$  is arbitrary, and  $\Phi$  is either determined by Poisson's equation or set to  $T$ . This makes the corrected satellite field noisy in both time and space. This was better tolerated in the weekly OI than in a higher-resolution product such as the daily OI developed in this study.

An alternative method would be to use empirical orthogonal functions (EOFs) to fill in the sparse in situ data (e.g., see Smith et al. 1996). As described there, the spatial modes  $S_i(x)$  (of order  $i$ ) are determined from a SST analysis for a well-observed period. These modes are then fit to the observed data for each time  $t$  to

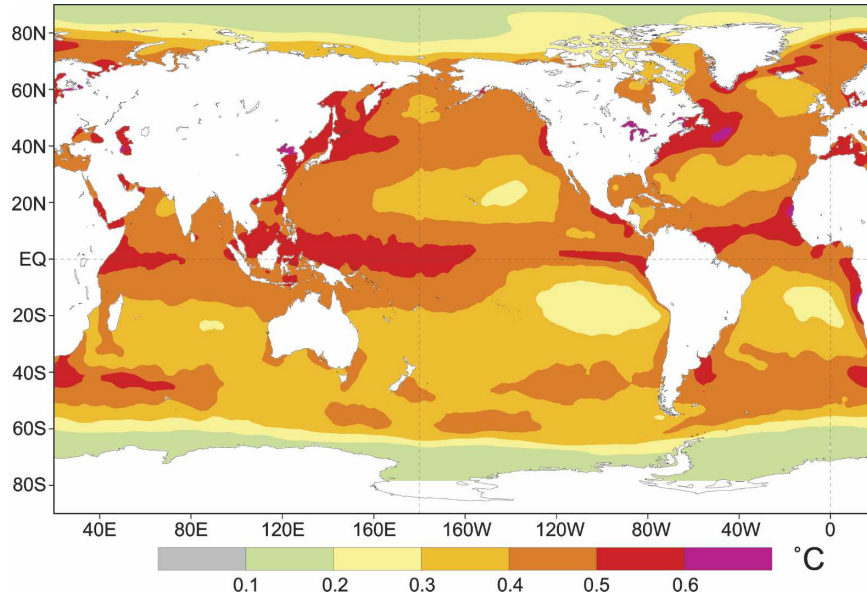


FIG. 6. Analysis increment standard deviation for 1985–2005 for the AVHRR-only daily OI. The analysis increment is the analysis minus the first guess. The standard deviation is assumed to be the OI sampling and random error if there are no observations.

determine the weights  $W_i(t)$  of each mode. The problem with this procedure (Smith et al. 1996) is that data tends to become sparser in the early part of the record. Thus, a mode can be generated with artificially large weights if the data coverage is poor for that particular mode. Smith et al. (1998) developed a method that objectively determines which modes can be supported by any designated data coverage. However, this method may fail if the mode has large spatial teleconnections. For example, if the magnitude of  $S_i(x)$  is large in both the Atlantic and the Pacific, the mode could be adequately sampled in Atlantic but not in the Pacific. If this problem occurred, the Pacific part of the mode would be extrapolated and may not be accurate. Because the EOF method demands orthogonality between modes, higher order modes tend to be spatial complex over large regions. Rotated modes are generally more localized and more closely resemble observed structures than unrotated modes (Richman 1986). Empirical orthogonal teleconnection (EOT) functions (Van den Dool et al. 2000) also produce modes with localized spatial functions. Furthermore, as discussed below, EOTs can be tuned to eliminate large teleconnections.

A new bias correction method was designed using EOTs. These functions were determined for a dataset,  $\Omega(x, t)$ , a function of space and time, by finding the location with the largest spatial covariance with respect to all the other points (see Van den Dool et al. 2000 for details). The time series at that point is defined as  $T_1(t)$ . By regression, the corresponding spatial function,  $X_1(x)$ ,

is then computed. The product of  $X_1(x) T_1(t)$  is subtracted from  $\Omega(x, t)$  and the process is repeated. This yields a set of modes such that  $\Omega(x, t) \approx \sum_{i=1}^M X_i(x) T_i(t)$ , where  $M$  is the maximum number of modes.

Smith and Reynolds (2003) used the OI.v2 SST anomalies to define  $\Omega(x, t)$  and determined a set of  $X_i(x)$  spatial modes, where  $M$  was set to 130. The number of modes,  $M$ , and the spatial functions,  $X_i(x)$ , was determined by Smith and Reynolds (2004). The value of  $M$  was selected subjectively to account for most of the global anomaly variations. Because of the way the modes were selected, the higher order modes tend to be spatially more coherent than unrotated EOFs. This can be seen in Fig. 7 where three modes (1, 4, and 100) are shown. Note that the spatial scale of mode 100 is roughly similar to the other modes. The major advantage of EOTs is that modes are determined one at a time. Thus, the individual modes can be tapered so that the maximum spatial extent of the mode is limited. Smith and Reynolds used linear tapering to limit the maximum extent of their functions to 800 km to avoid large spatial teleconnections.

To avoid situations in which a mode is only sampled outside of its center of action, Smith and Reynolds (2003) defined a mode selection criteria,  $C_i$ , given by

$$C_i = \frac{\sum_x \delta(x) X_x^2(x) \alpha(x)}{\sum_x X_x^2(x) \alpha(x)}, \quad (7)$$

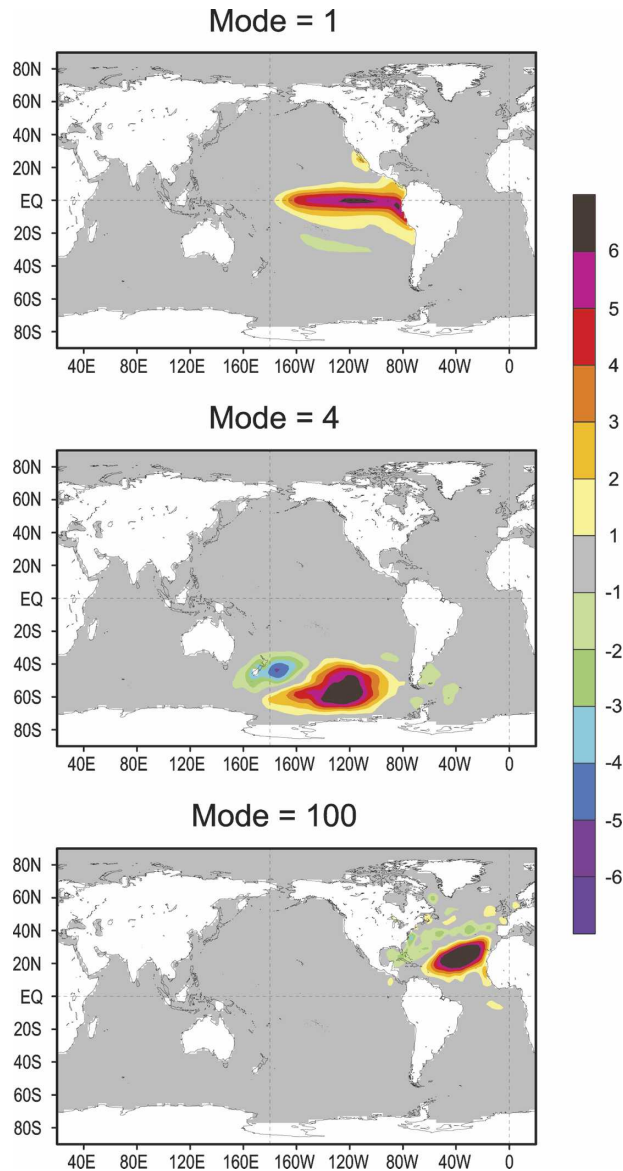


FIG. 7. Empirical orthogonal teleconnection spatial modes: modes 1, 4, and 100. The EOT method used here avoids basin-scale teleconnections.

where  $\delta(x)$  is 1, if there are observations at grid location  $x$ , or 0, otherwise, and  $\alpha(x)$  is the cosine weighting of the area associated with each  $2^\circ$  grid box. If  $C_i$  is below a critical threshold, the data are considered to be inadequate and the mode is not used. Smith and Reynolds carried out cross-validation studies and determined that this critical threshold must be at least 15% for adequate sampling. The modes that satisfy this critical sampling test are used and are fit to in situ SST data as described in Smith et al. (1996) to define the anomalies; otherwise, the modes are not used.

The EOT spatial modes of SST anomalies were used

to bias correct the satellite data. In this procedure seven days of in situ data and satellite data were converted into anomalies and then separately averaged onto a  $2^\circ$  grid. Because it is important to use the same modes for both sets, modes were only selected if  $C_i$  for both sets was greater than 15%. In almost all cases, modes like mode 4 (Fig. 7) were not used. Mode 4 could be represented by the satellite data but not by the in situ data because of the lack the in situ data there. (If, for example, mode 4 were used, the large-scale in situ anomaly from the mode would be zero, and the large-scale smoothed satellite anomaly would be treated as a bias and eliminated.) Next, the temporal factors were determined for the modes used for each set of anomalies. The difference between the two reconstructed EOT fitted fields was then computed as the bias adjustment. The adjustment was interpolated to the OI  $1/4^\circ$  grid and used to correct each satellite superobservation. This method was applied separately for day and night and for each satellite instrument. The corrected satellite data were then used in the daily OI.

The EOT bias adjustment method has the additional important advantage that it can be used to define an estimate of the bias error. This is done by assuming that the satellite bias error is related to satellite EOT modes, which could not be corrected by the in situ data plus a residual. The individual EOT bias variance,  $E_{Bj}^2$ , is

$$E_{Bj}^2 = \sum_{i=1}^M \Delta_{ij} X_i^2(x) \sigma_i^2, \quad (8)$$

where  $j$  is an index for the number of satellite sources used. The factor  $\Delta_{ij}$  is 1 if the mode was not adequately sampled by either the satellite or the in situ data; otherwise, it is 0. The bias variance associated with each mode is  $\sigma_i^2$ , which was estimated by computing the satellite reconstructed anomaly modes for 1985–2005 and then determining the variance of each mode. The anomaly variance was found to be similar to the bias variance for those modes adequately sampled, allowing the bias variance of those modes to be computed. The values of  $\sigma_i^2$  generally decrease with increasing value of the index  $i$ . Equation (8) is probably an overestimate of the EOT bias error because the modes are almost, but not completely, orthogonal. Thus, the nonorthogonal overlap of modes can count the variance in some regions more than once, giving an overestimate.

The total bias error  $E_B^2$  can be expressed as

$$E_B^2 = E_{B0}^2 + \frac{1}{mn} \sum_{j=1}^N E_{Bj}^2, \quad (9)$$

where  $n$  is the total number of sets of satellite data used for which biases are estimated by (8),  $m$  is the number

of independent satellite instruments, and  $E_{B0}^2$  is the residual error variance for the bias not resolved by the modes. The value of  $E_{B0}^2$  was set equal to  $0.01^\circ\text{C}^2$ . This value was estimated by examining residual differences between AMSR and AVHRR and by the residual difference between ships and buoys.

In (9), day and night observations from the same satellite have been assumed to be dependent data, while observations from different satellite are independent. Thus, if just AVHRR day and AVHRR night are used,  $m = 1$  and  $n = 2$ , and  $E_{Bj}^2$  from the two satellite sources is simply averaged. However, if AMSR day, AMSR night, AVHRR day, and AVHRR night are used,  $m = 2$ ,  $n = 4$ , and  $E_{Bj}^2$  from all four satellite sources is averaged and then divided by 2. In this case the average bias is reduced because two independent satellite sources are used. Note that the modes defined by  $\Delta_{ij}$  in (8) may be different at the same time step because the satellite data distribution can vary even though the in situ distribution is the same. However, for the 7-day period used for the bias adjustment, all modes can usually be expressed by the satellite data alone; thus,  $\Delta_{ij}$  is usually the same.

The total error variance assumes that the random and sampling error and the bias error are independent and is therefore simply the sum of  $E^2$  from (6) and  $E_B^2$  from (9) at each grid point. The total error (standard deviation) is shown in Fig. 8. The large scale patterns south of  $40^\circ\text{S}$  are primarily due to the bias errors due to limited in situ data. The bias errors are lower for AMSR and AVHRR than for AVHRR only because two independent satellite instruments were used in the AMSR and AVHRR OI. The random and sampling errors are indicated in the figure by north/south bands in the error magnitude. Here the higher values occur in regions between the satellite swaths. In the regions with data, the random and sampling errors are very small because of the dense satellite coverage. The sampling and random errors are even lower when AMSR is added to AVHRR data, as also shown in Fig. 8.

### c. The computation

With the EOT bias and OI steps complete, the daily OI was run with EOT bias correction using Pathfinder AVHRR data (3 January 1985–31 December 2005) and operational AVHRR data (1 January 2006 to present). The second daily OI product used the AVHRR data plus the AMSR data, which began in June 2002. These two daily OI products are designated as the daily OI, version 1. (The version number is not continued from the weekly OI because the daily OI has greatly expanded temporal and spatial resolution compared to the weekly product.) Other special products were also

run for the comparisons that follow. These include the above analyses using uncorrected satellite data as well as a special AMSR-only analysis.

## 4. Results

In this section, the new daily OI analyses products are intercompared with themselves and other products.

### a. SST gradient intercomparisons

The first step was to recompute the SSTs and SST gradients for the six regions considered by CW05 with the addition of the daily OI using AVHRR and AMSR and AVHRR. Because gradients are computed from spatial differences, they are useful in showing how well analyses can resolve strong coherent features.

Figure 9 shows the magnitude of the 3-day mean Gulf Stream SST gradients centered on 1 October 2003. AVHRR data show high-resolution details in cloud-free regions, although the coverage for AVHRR data is less than half of the possible number of ocean grid points. AMSR data show smoother details because of the coarser footprint but with the expected better coverage except near land as AMSR SSTs cannot be retrieved within 75 km of land. The analyses fill in the missing AMSR and AVHRR data gaps with different smoothing. In particular, note the region of missing AMSR data due to precipitation contamination between  $35^\circ$  and  $45^\circ\text{N}$  along  $60^\circ\text{W}$ . Here the AMSR and AVHRR daily OI correctly fills in the missing data. This procedure is not always done correctly, as will be shown below. In the comparison, the OI.v2 is heavily smoothed, as reported by CW05. The RTG\_SST and AVHRR OI are similar, showing much more detail. Here the RTG\_SST is slightly smoother than the AVHRR OI. The highest resolution is obtained by the AMSR and AVHRR OI, which is similar to the AMSR data in most of the offshore regions. The improvement in the AMSR and AVHRR analysis resolution is due to the better AMSR coverage compared to AVHRR. The results for other western boundary currents (e.g., the Agulhas, the Kuroshio, and Falkland Current regions, not shown) show the same rankings of gradients for the SST products and data.

The mean SST gradient is shown for the tropical eastern Pacific region for the 3-day period centered on 28 May 2003 (Fig. 10). The overall analysis gradient ranking is again the same. In this case, the AVHRR-only OI gradient resolution is almost as good as the AMSR–AVHRR OI. This is because the overall percent of AVHRR oceanic data coverage in Fig. 10 is larger than the AVHRR coverage in Fig. 9.

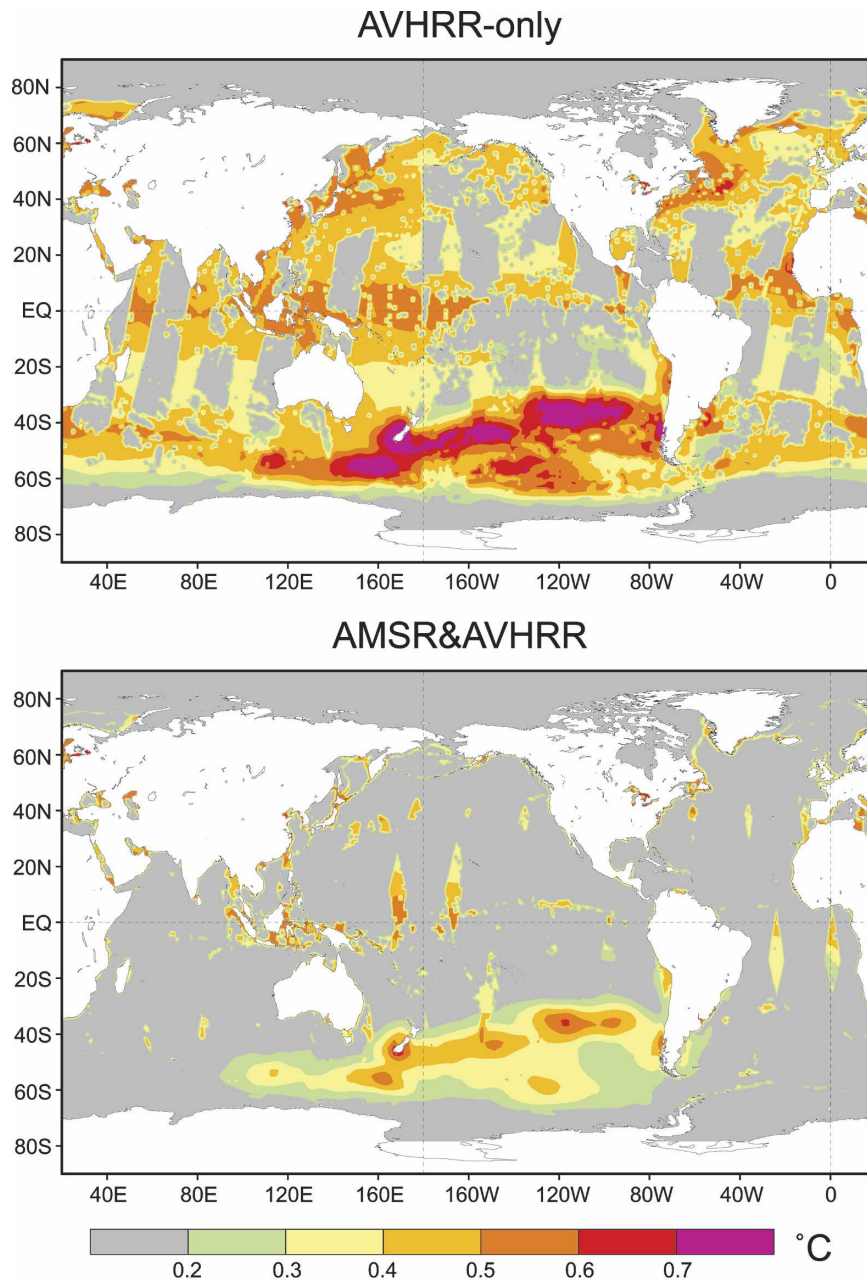


FIG. 8. Total error (standard deviation) for 1 Jan 2003 for (top) the AVHRR-only and (bottom) AMSR and AVHRR combined analyses. The total error is derived from the random, sampling, and bias error (see text).

At first it may seem surprising that the OI AVHRR gradients are as accurate as is shown, given the relatively sparse availability of AVHRR data due to cloud cover. Examination of the daily OI over time using AMSR data shows that most of the SST gradient features in western boundary currents vary relatively slowly. Because of the persistence built into the OI procedure by using the previous analysis as the first

guess for each new analysis, the daily OI using AVHRR alone does a credible job of determining much of the signal with only limited observations, even in winter. However, in some high-gradient regions, such as the eastern tropical Pacific region (Fig. 10), the SST gradient patterns vary on shorter time scales and are not well resolved in the AVHRR-only OI during periods of persistent cloud cover.

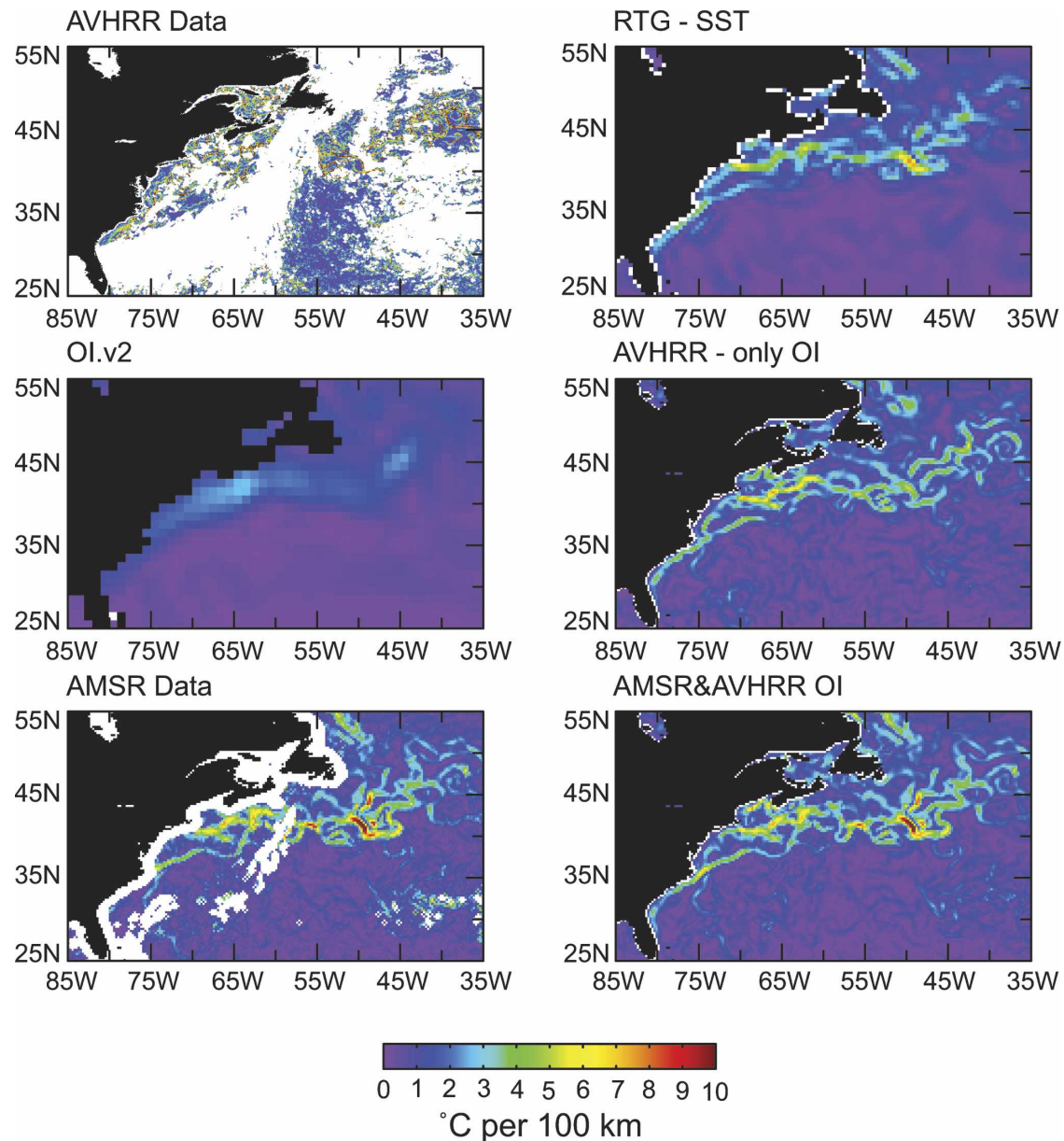


FIG. 9. Three-day averages of SST gradient magnitudes for analyses and data centered on 1 Oct 2003 for the Gulf Stream region. The data products are AVHRR and AMSR. The analyses are OI.v2, RTG\_SST, and the daily OI for AVHRR-only and AMSR and AVHRR. The analysis gradients are weakest for the OI.v2 and strongest for the daily OI using AMSR and AVHRR.

To investigate the gradients over time, gradient indices were computed. The index for the Gulf Stream was computed from the daily magnitude of the SST gradients from June 2002 through December 2004 for three daily OI runs: AVHRR-only, AMSR-only, and AMSR-AVHRR, and for the OI.v2 and RTG\_SST analyses. For the Gulf Stream, the maximum gradient value was determined along lines of longitudes from 70° to 40°W at intervals of 0.25° between 35° and 50°N;

these maximum values were then averaged over longitude and daily indices created (Fig. 11). The AMSR-only OI is not plotted because the differences between the AMSR and AMSR and AVHRR combined OI are very small and could not be distinguished. The results show that the OI.v2 SST gradients are consistently much weaker than the others, as expected (Fig. 9). Also as expected, the AVHRR-only and the RTG\_SST indices are generally quite similar. Perhaps the most in-

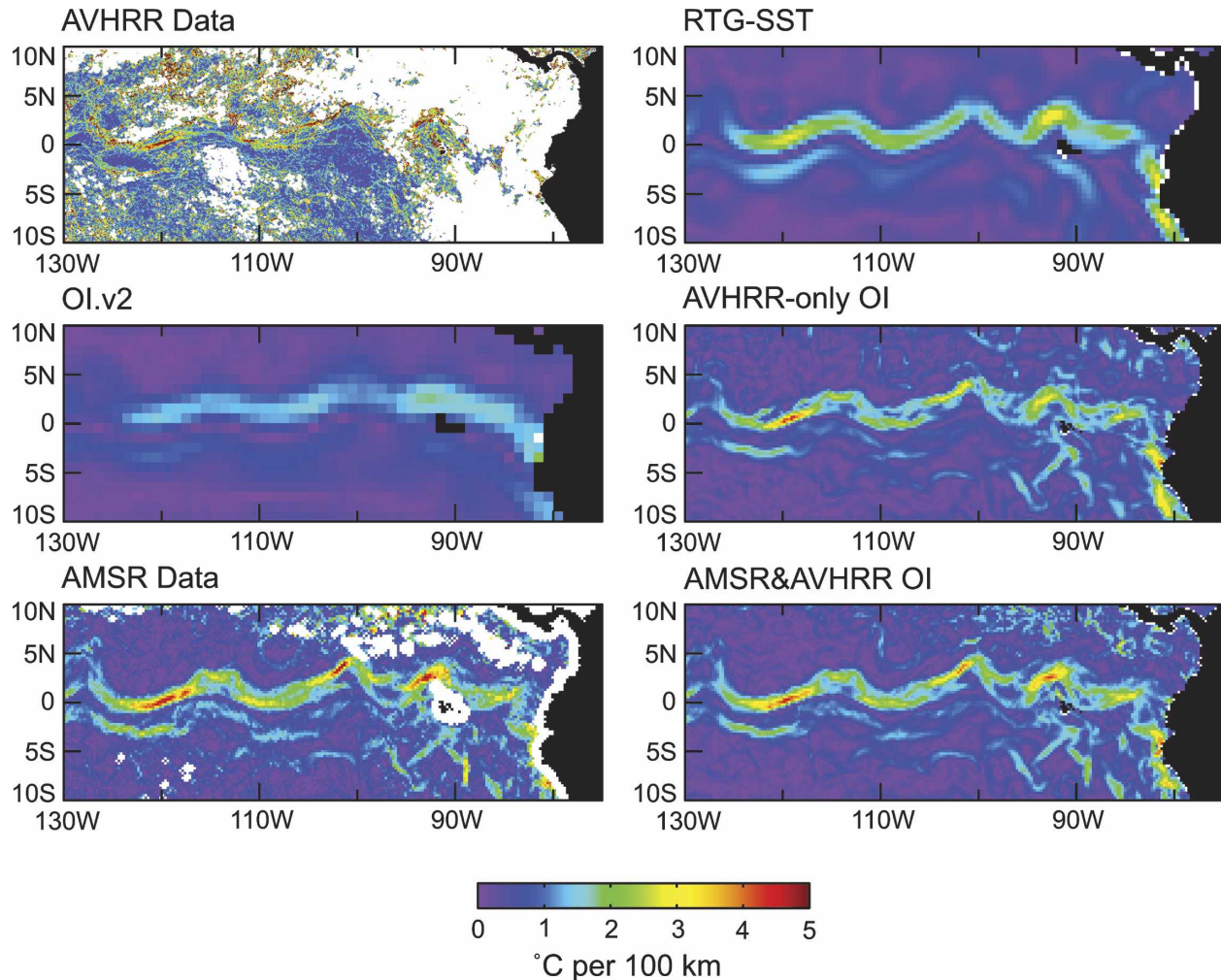


FIG. 10. Three-day average of SST gradient magnitudes for analyses and data centered on 28 May 2003 for the eastern Tropical Pacific; otherwise as in Fig. 9.

interesting difference occurs between the AVHRR-only and AMSR and AVHRR gradient indices. These indices are similar in August and September, with the AMSR and AVHRR gradient index only slightly stronger. The differences gradually increase from September to roughly March and then decrease again to the August minima. In winter, the AMSR and AVHRR gradient index is almost double the AVHRR-only index. The results show that the seasonal cycle of the index is underrepresented by AVHRR alone because cloud cover tends to be more pervasive in winter.

#### b. AMSR limitations

The benefits of the improved sampling from the near-all-weather measurement capability for MW are clear. Of course every satellite instrument has limitations, and it is useful to show a problem with the AMSR

data. One such problem is shown (Fig. 12) for the daily OI AVHRR and AMSR and AVHRR combined analyses and for AMSR data. The top panels show the SST and the bottom the gradients for a 3-day-average centered on 9 February 2003. There is a region of missing AMSR data near 25°N, 130°W. Because of the 3-day average and the irregular shape, the pattern is most likely due to precipitation, which contaminates the AMSR SST retrievals. The AMSR and AVHRR OI analysis fills in the missing data. In this case, AVHRR data cannot compensate for the missing AMSR data because of the associated cloud cover. The problem is most evident in the SST gradient panels because the spatial derivatives magnify the “edge effects” of the precipitation contamination. To correct this problem, AMSR data near the edge of regions with precipitation contamination data should be excluded in future versions of the OI.

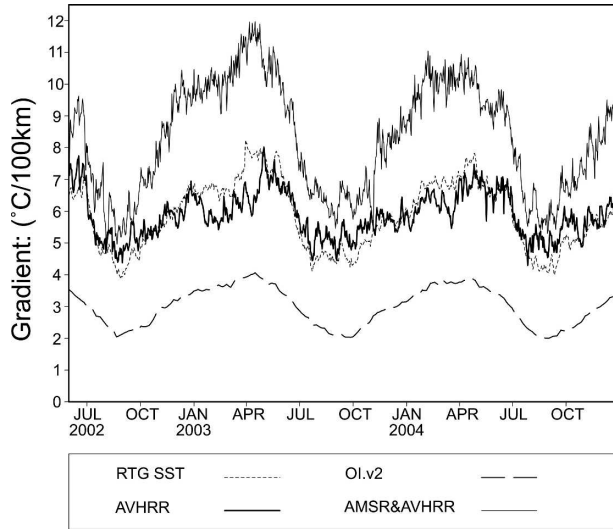


FIG. 11. Analysis SST gradient index (see text) for the Gulf Stream region for 1 Jun 2002–31 Dec 2004. The analyses are the OI.v2, the RTG\_SST, and the daily OI using AVHRR-only and AMSR and AVHRR. Gradients are weakest for the OI.v2. The near-all-weather coverage of AMSR improves the winter and spring gradients of the daily AMSR and AVHRR OI over analyses using AVHRR alone.

### c. Day-to-day differences

Both versions of the daily OI show day-to-day differences. These differences are especially evident in regions of high variability (e.g., the Gulf Stream region in winter). Figure 13 shows one day of AMSR and AVHRR day and night data anomalies on a  $0.25^\circ$  spatial grid for 11 January 2003. The figure shows the improved coverage of AMSR over AVHRR. Cloud cover restricts the potential AVHRR coverage, while precipitation restricts the AMSR coverage. However, all data anomalies show sampling difficulties. In particular, the AMSR daytime anomalies are warmer than for AMSR night south of  $30^\circ\text{N}$ , suggesting a diurnal warming. However, north of  $50^\circ\text{N}$  between  $50^\circ$  and  $40^\circ\text{W}$ , nighttime AMSR is warmer than daytime. Given four snapshots of a complex and variable SST field over one day, it should not be surprising that four partly obscured snapshots show inconsistencies when compared with each other. To reduce these differences, a 3-day data window with appropriate temporal  $e$ -folding error correlation scales may need to be added to a future version of the daily OI.

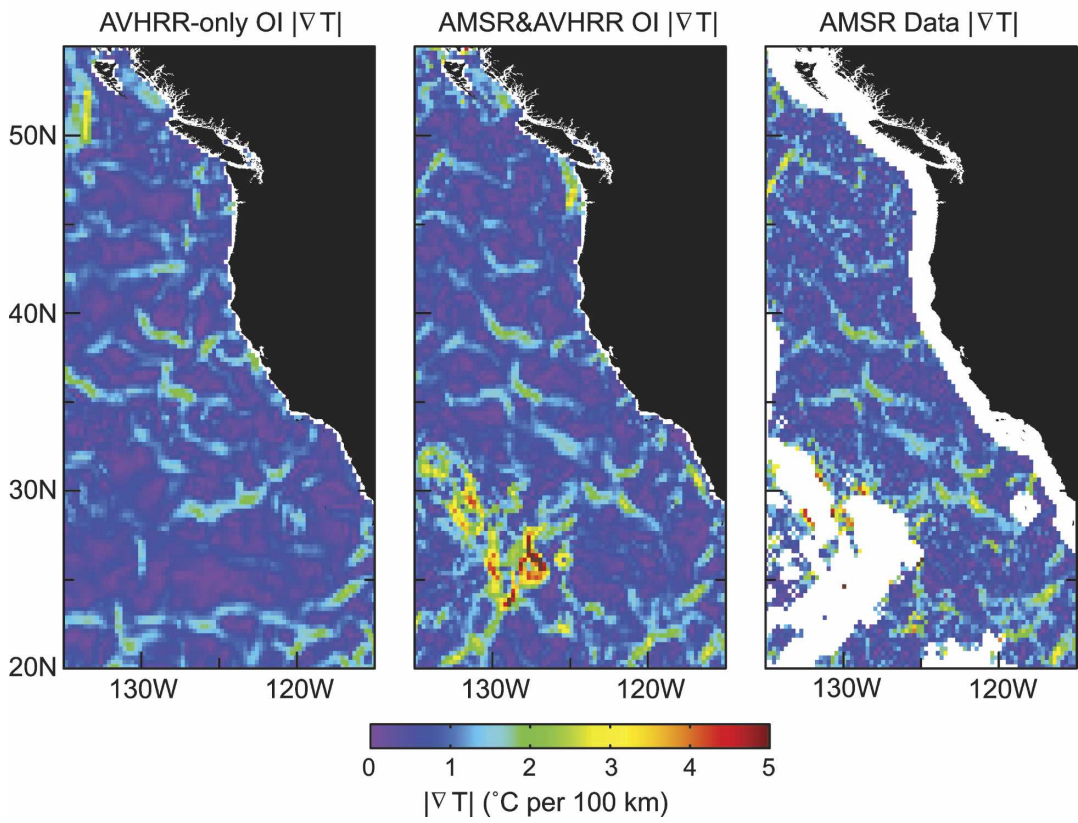
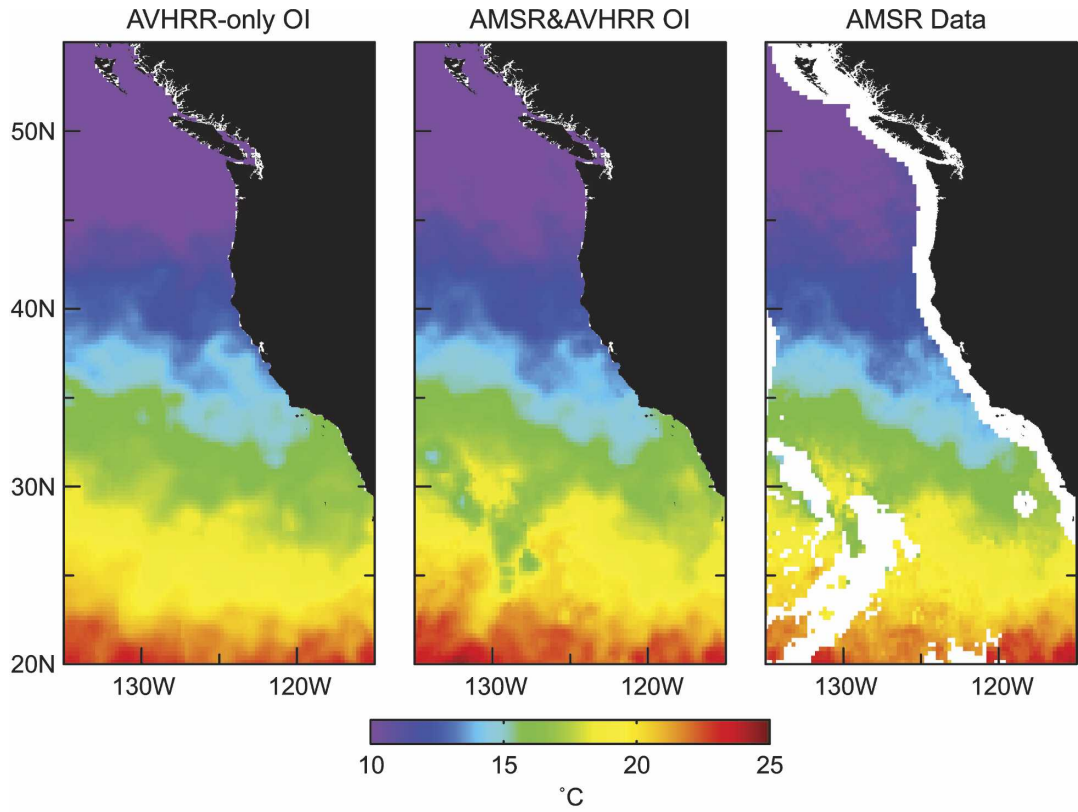
### d. SST bias adjustments

Finally, the large-scale biases for the January 2003–December 2005 period are now examined where the AMSR and AVHRR combined daily OI analysis is used as a reference. The average difference with re-

spect to the AMSR and AVHRR is computed for this period for the OI.v2, the AVHRR-only daily OI with and without bias correction, and the AMSR and AVHRR daily OI without bias correction. For this comparison, the OI.v2 is linearly interpolated to the daily OI grid. The OI.v2 (top-left panel in Fig. 14) shows that the biggest difference with respect to the AMSR and AVHRR daily OI occurs between  $60^\circ$  and  $40^\circ\text{S}$ , with largest values in the Pacific east of the date line. This is the region of the World Ocean with the poorest in situ data coverage (see Reynolds et al. 2002); thus, the true bias is not well known. Many of the other differences in the western boundary current regions (e.g., in the Gulf Stream and Kuroshio) and in the eastern Pacific equatorial region are due to the increased resolution of the daily OI. The AVHRR-only OI with bias correction (top-right panel) shows some residual biases with respect to the AMSR only AVHRR daily OI primarily along the ITCZ and SPCZ, a reminder that residual biases can survive the bias correction step if the biases persist (Fig. 1).

The AVHRR-only OI analysis without bias correction (bottom-left panel in Fig. 14) shows the largest biases with respect to the AMSR and AVHRR combined analysis with bias correction. The biases are especially evident in tropical oceans. Comparison with the AVHRR-only OI analysis with bias correction (top-right panel) shows the necessity of the bias correction. The AMSR and AVHRR OI analysis without bias correction (bottom-right panel) with respect to the AMSR and AVHRR analysis with bias correction shows smaller long-term biases although some biases remain as discussed below.

The daily OI biases in the Tropics can be evaluated using the Tropical Atmosphere–Ocean (TAO) moored buoy array (McPhaden et al. 1998). These data are used in all daily OI analyses and in the RTG\_SST and the OI.v2. Zonal sections of the average analysis anomalies for 2003–05 (Fig. 15) along  $5^\circ\text{N}$  show the daily AVHRR-only and AMSR and AVHRR OI analyses with and without bias correction where the OI.v2 analysis is shown for reference. The AMSR and AVHRR combined analyses generally agree with the OI.v2. The two AVHRR-only OI analyses show the original bias from the uncorrected AVHRR Pathfinder data and a residual bias from the corrected Pathfinder data. In addition to the expected results (Fig. 15), positive spikes can be seen in the two AVHRR-only analyses. Locally these spikes tend to move the analysis toward the OI.v2 and the AMSR and AVHRR analyses. The spikes are due to the combination of in situ data from the TAO array and the AVHRR pathfinder data. Near the location of the mooring, both types of observations are



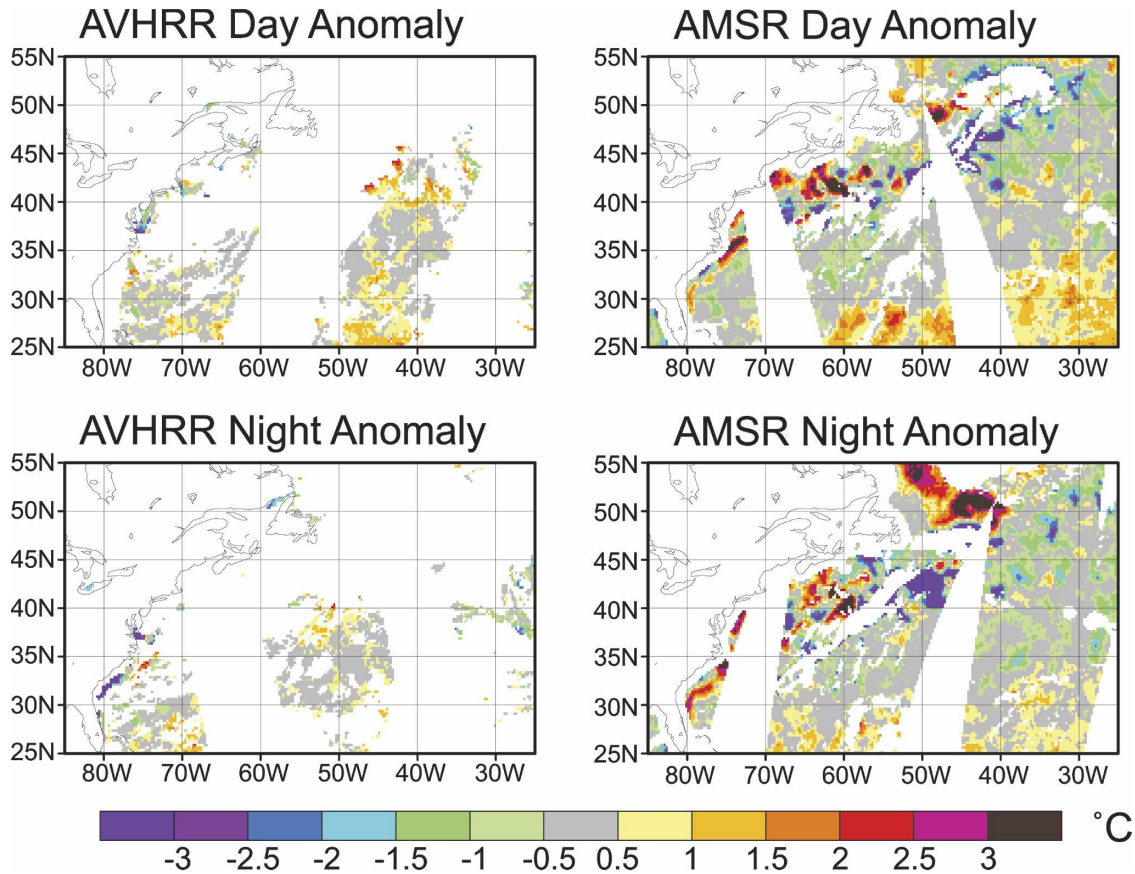


FIG. 13. Daily daytime and nighttime data anomalies for (left) AVHRR Pathfinder and (right) AMSR for 11 Jan 2003. Note the sampling variability among the four panels. The same climatological field is used to compute all the anomalies shown because the climatology does not include any diurnal signal.

used: away from these locations, the moored data have little impact, as can be expected from the spatial scales in Fig. 4. The amplitudes of the spikes are roughly  $0.10^{\circ}$ – $0.15^{\circ}\text{C}$  for the AVHRR-only analysis with corrected AVHRR data and  $0.20^{\circ}$ – $0.40^{\circ}\text{C}$  for the AVHRR-only OI analysis without bias correction. It is important to note that these spikes would have been smoothed in the OI.v2 if they had occurred. For the user of any high-resolution SST analysis, it is critical to realize that a high-resolution analysis shows both an increased signal and a greater susceptibility to noise. Furthermore, the analysis differences shown in the top panel (Fig. 15) help justify the  $0.01^{\circ}\text{C}^2$  residual bias variance assumed in section 3.

Both the AVHRR-only and the AMSR and AVHRR daily OI analyses without bias correction have a mid-latitude Northern Hemisphere bias (Fig. 14) with respect to the AMSR and AVHRR daily OI with bias correction. Although biases are corrected, the fact that both uncorrected IR and MW products have similar biases suggests that these biases may be due to biases within the in situ data, themselves.

## 5. Summary and discussion

A set of higher resolution SST analyses have been produced using OI. The analyses have a spatial grid resolution of  $0.25^{\circ}$  and a temporal resolution of 1 day.

←

FIG. 12. Three-day averages of analyses and data centered on 9 Feb 2003 for an area off the west coast of North America: (top) The daily OI SSTs for AVHRR-only and AMSR and AVHRR and for AMSR data and (bottom) the associated SST gradient magnitudes. Precipitation reduces the AMSR data coverage over a region centered on  $25^{\circ}\text{N}$ ,  $130^{\circ}\text{W}$ . Contamination of AMSR SSTs near the edge of the precipitation boundary leads to interpolation errors in the daily OI.

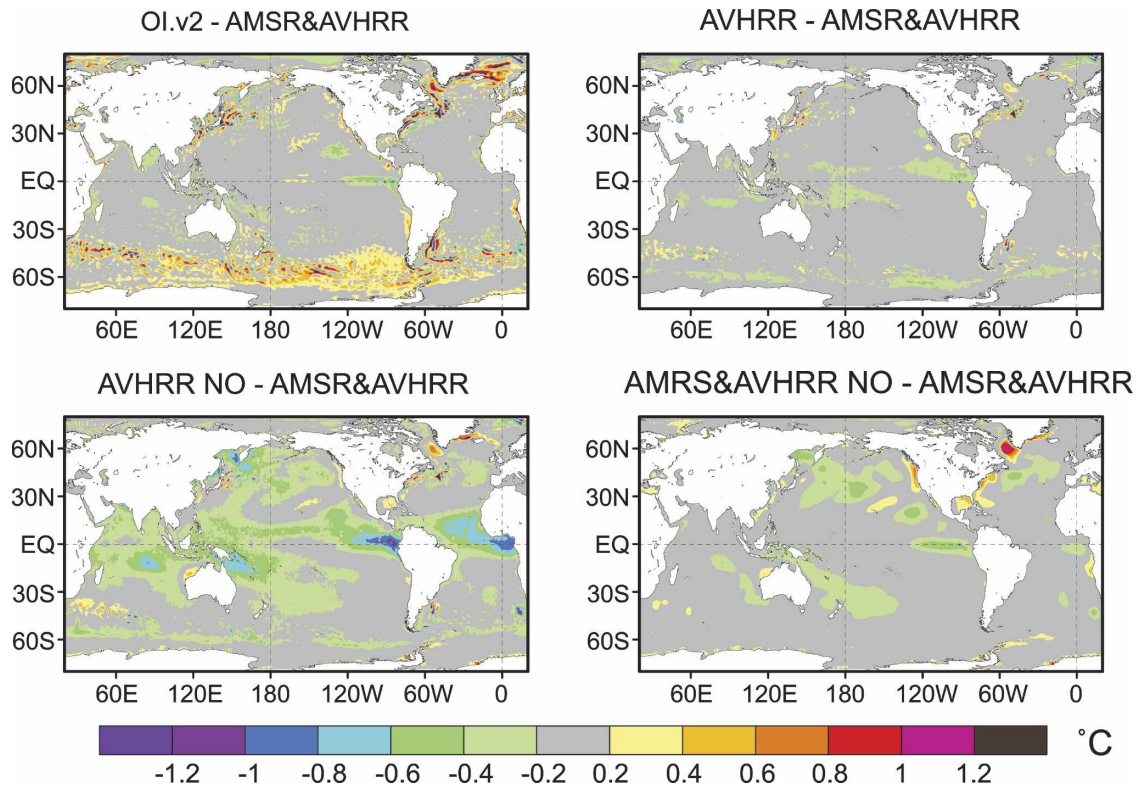


FIG. 14. Average analysis differences for 2003–05 with respect to the daily OI AMSR and AVHRR with bias correction. (top) The analyses compared with bias correction are the AVHRR-only daily OI and the OI.v2. (bottom) The analyses without bias correction are the AVHRR-only and the AMSR and AVHRR daily OI. “No” in the title indicates no bias correction. (bottom left) The daily OI AVHRR-only without bias correction shows the largest difference with respect to the daily OI AMSR and AVHRR with bias correction.

One product uses satellite IR data from AVHRR. The other uses AVHRR and satellite MW data from AMSR. Both products use in situ data and include a large-scale adjustment of the satellite biases with respect to the in situ data. The results show that both products have dramatically improved spatial and temporal resolution compared to the weekly OI.v2 analysis (Reynolds et al. 2002). Infrared instruments can produce SST retrievals only during cloud-free periods, while MW can produce SST retrievals except within 75 km of land and during precipitation events. The mid- and high-latitude MW coverage, especially in winter, is far superior to the IR coverage, although the IR spatial resolution is much better than MW when skies are clear. Because of the improved coverage of the MW data, the analyses show a strong increase in variance and SST gradient resolution when AMSR became available in June 2002. Therefore, two products have been produced: an AVHRR-only product dating back to January 1985 and an AMSR and AVHRR combined product dating back to June 2002.

The AVHRR-only product uses Pathfinder AVHRR data (currently available from January 1985 to December 2005) and Operational U.S. Navy AVHRR data from 2006 onward. Pathfinder AVHRR data were chosen over operational AVHRR data because they had lower large-scale variability with respect to in situ data. Systematic biases nonetheless remain in the Pathfinder AVHRR data, which are not completely corrected by the EOT bias correction procedure applied here (Figs. 1 and 14). Furthermore, the operational AVHRR data used in 2006 includes multiple AVHRR instruments, whereas Pathfinder AVHRR presently includes only one instrument for any given part of the record. Pathfinder AVHRR data could be improved in the later part of the record by providing Pathfinder products for all available AVHRR instruments. Also, the Pathfinder AVHRR data do not include the local time of the observation since they are produced by binning observations into a temporal (as well as spatial) grid. Further improvement in AVHRR data would be useful for improving the accuracies of the OI analyses produced here.

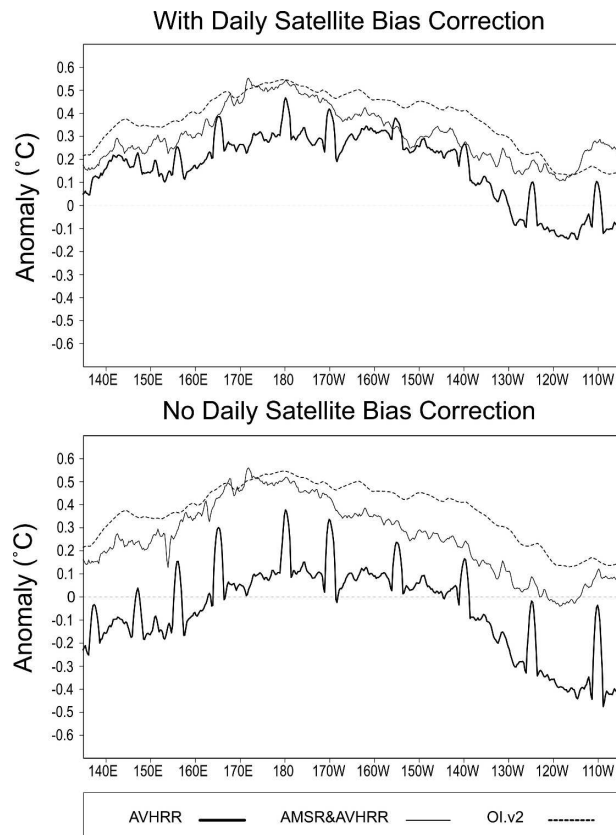


FIG. 15. Average analysis anomalies for 2003–05 along 5°N in the Pacific. The daily analyses are the AVHRR-only and AMSR and AVHRR (top) with and (bottom) without bias correction. The OI.v2 analysis is shown for reference. The spikes in the daily OI AVHRR-only analyses show the local balance of the TAO buoy and satellite SSTs on the analysis.

The AMSR and AVHRR combined product begins with the start of the AMSR data record in June 2002. The improved coverage from AMSR leads to improved spatial resolution of SST gradient features compared with the AVHRR-only product (Figs. 9–11). In the AMSR and AVHRR product, the primary AVHRR contribution is near land. Of course AVHRR could further improve the resolution in cloud-free regions. However, the resolution of an AVHRR-only analysis is degraded during cloudy periods (Fig. 11).

Because their error characteristics are independent and systematic biases may tend to cancel each other, there is an important advantage in using both IR and MW instruments. However, problems remain near edges of precipitation boundaries where errors in AMSR SST retrievals cannot be compensated by IR data because of cloud cover (Fig. 12).

(The daily OI SST analyses are presently available via FTP at <ftp://eclipse.ncdc.noaa.gov/pub/OI-daily/>,

TDS at <http://nomads.ncdc.noaa.gov:8085/thredds/catalog.html>, and LAS at <http://nomads.ncdc.noaa.gov:8085/las/servlets/dataset>. The Web server address is <http://www.ncdc.noaa.gov/oa/climate/research/sst/oi-daily.php>.)

Further work is needed and will continue. One of the most important steps is to develop a method to improve the bias correction and to correct ship and buoy biases. In addition, the data time window may need to be opened to 3 days to eliminate day-to-day noise (Fig. 12). [C. Gentemann (2006, personal communication) has recently added additional precipitation flags to the AMSR data that may mitigate the precipitation edge effects noted above.] As improved satellite AMSR and AVHRR datasets become available, the analyses will be reprocessed. One of the most important potential improvements would occur due to the addition of new satellite datasets. The next daily OI product will include the MW Tropical Rainfall Measuring Mission (TRMM) Microwave Imager (TMI) (which samples between 38°S and 38°N) and the global Along Track Scanning Radiometer (ATSR) series of IR instruments. Later additions will include other polar and geostationary data. Each of these satellite datasets will first be examined separately using an independent analysis. It is hoped that the number of final products will not have to be expanded. New products will only be added when, as expected, the SST analyses show a significant improvement with the addition of new satellite. Improvements with updated documentation will be added as needed.

*Acknowledgments.* We are grateful to NCDC and the NOAA/Office of Global Programs, which provided partial support for this work. The graphics were computed using the Grid Analysis and Display System (GrADS, available online at <http://grads.iges.org/grads>), Center for Ocean–Land–Atmosphere Studies. We thank the following people for help with the data: Diane Stokes for providing information and access to real-time in situ data and sea ice data, Chelle Gentemann for providing information about the AMSR-E data, and John Sapper for providing real time access to the AVHRR data. Reynolds thanks the Cooperative Institute for Oceanographic Satellite Studies at Oregon State University (OSU) for contributing part of his travel costs towards a visit to OSU in July 2005. NOAA reviewers Sharon LeDuc, Gary Wick, and Huai-Min Zhang provided helpful editorial comments. Further constructive comments were obtained from an anonymous reviewer, as well as Chris Folland, and Alexey Kaplan.

## APPENDIX A

## Simulating SSTs from Sea Ice Concentration

The quadratic (1) and linear (2) equations defined in section 2c express the relationship between sea ice concentration and SST. In this appendix the two equations were examined to determine the differences between the equations and to estimate a minimum sea ice concentration for use with (1) and (2). The coefficients  $a$ ,  $b$ ,  $c$ ,  $b'$ , and  $c'$  in (1) and (2) were determined by regression for  $30^\circ$  wide longitude bands (or sectors) for each month for the Northern and Southern Hemispheres. In addition, there were four separate  $30^\circ$  wide bands for the North Pacific south of  $66^\circ\text{N}$  and one each for the Baltic Sea and Great Lakes. These extra regions were necessary because the sea ice in these regions behaves differently than the general Northern Hemisphere bands at the same longitudes. Both the linear and quadratic constants were determined by a climatological least squares fitting procedure using collocated SST data (AVHRR and in situ) and sea ice concentrations with the constraint that the simulated SST is set to the freezing point of water ( $-1.8^\circ\text{C}$  for the ocean or  $0^\circ\text{C}$  for the Great Lakes) when the sea ice concentration is 1. Once this is done, the sea ice concentration, location, and month can be used to generate the simulated SST.

In the OI.v2, sea ice concentrations were bias adjusted following the procedure in Rayner et al. (2003) to account for melt pond summer biases. This adjustment was done to smooth the transition between satellite and in situ–derived ice concentrations in the OI.v2. However, it was not needed here because in situ–derived sea ice concentrations were not used and because the fitting procedure in (1) and (2) accounts for any local biases via the derived coefficients.

To determine whether Eq. (1) or (2) is more accurate and to determine the minimum value the coefficients were determined by a regression of observed SSTs (satellite and in situ) onto observed sea ice concentrations for a 10-yr-dependent period (1985–94). The accuracy of the regression was evaluated for an independent period (1995–2004). For this independent period, biases and rms differences were computed between simulated SSTs generated from sea ice concentrations and actual observed SSTs. These biases and rms differences were computed for ice concentration bins with widths of 0.1 centered on multiples of 0.1.

Figure A1 shows a summary of the rms differences and biases averaged over all months and all Northern Hemisphere regions. The rms differences are noisy and not very useful in determining whether (1) or (2) is more accurate. The results do show that rms errors

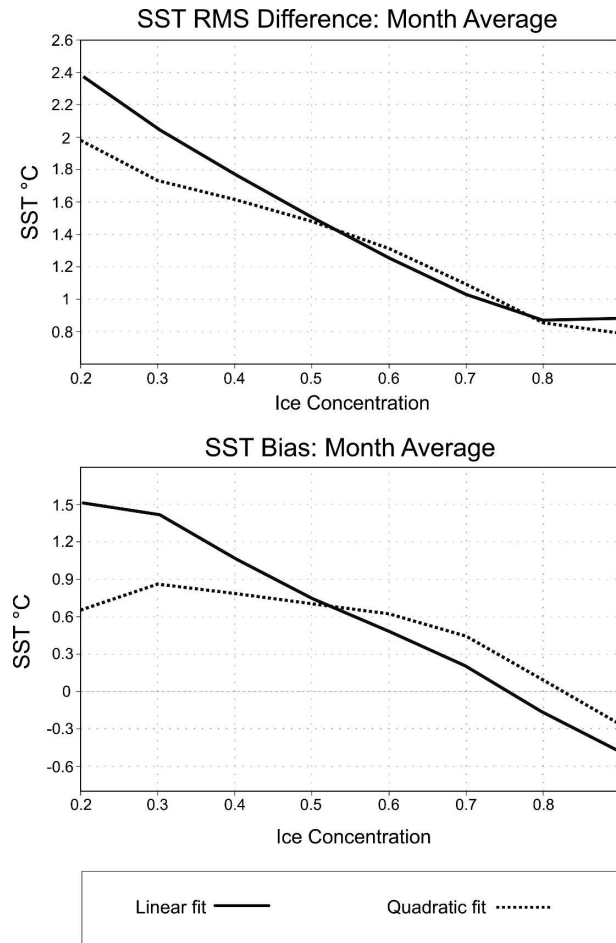


FIG. A1. Northern Hemisphere average (top) rms difference and (bottom) bias between measured SSTs minus SSTs simulated from sea ice concentration for all months for quadratic and linear fits. The period for the comparison is 1995–2004, an independent period.

increase with decreasing concentration. This should not be surprising since climatology is used to generate the SSTs and the only constraint in the fit occurs at high concentrations (i.e., at the freezing point of the water). However, the differences in the biases did have useful information. A perfect fit would have zero biases. The results indicate that the absolute biases are smaller for the linear fit for ice concentration bins between 0.6 and 0.7 and smaller for the quadratic fit for the 0.9 bin and for bins less than 0.5. At bins of 0.5 and 0.8, the fits are about equal. Furthermore, for some quadratic fits (not shown) data are sparse and the quadratic fit may generate SSTs that are unstable at low sea ice concentrations and may generate extreme SSTs there. As a conservative approach, the minimum sea ice concentration for use of (1) or (2) was set to 0.5 and the linear fit (2) was selected over the quadratic fit. This limits the maxi-

mum rms error to less than 1.5°C. Thus, SSTs were simulated for sea ice concentrations  $\geq 0.5$  using (2); no SSTs were simulated for sea ice concentrations  $< 0.5$ .

## APPENDIX B

### Combining Observations Using Simplified Optimum Averaging

This appendix discusses a simplified optimum averaging (OA) appropriate for combining observations, and also for computing the error estimate of the combination. For reference and background, see section 3.3 in Kagan (1979).

To begin, Kagan's Eq. (3.3.2) is used and rewritten here as

$$\sum_{i=1}^n w_i C_{ij} + w_j E_j^2 = C_{jA}, \quad j = 1, \dots, n, \quad (\text{B1})$$

where  $C_{ij}$  is the covariance between observations  $i$  and  $j$ ,  $C_{jA}$  is the covariance between observation  $j$  and the average value, and  $E_j^2$  is the noise error variance of observation  $j$ . The OA weights for the  $n$  observations are  $w_j$ .

Here the averaging region is assumed to be the OI analysis 0.25° spatial box. For this box it is assumed that the averaging region is small enough that all correlations within the region are equal to 1 and that the variance,  $\sigma^2$ , is constant within the region. With these assumptions, the OA weights for the  $n$  individual observations are found by solving

$$\varepsilon_j^2 w_j + \sum_{i=1}^n w_i = 1, \quad j = 1, \dots, n. \quad (\text{B2})$$

In (B2),  $\varepsilon_j^2 = E_j^2/\sigma^2$  is the noise-to-signal variance ratio of observation,  $j$ .

From (B2) the weights can be expressed as

$$w_j = \frac{1 - \sum_{i=1}^n w_i}{\varepsilon_j^2}. \quad (\text{B3})$$

The sum of the weights is then

$$n\bar{w} = \sum_{i=1}^n w_i = (1 - n\bar{w}) \sum_{j=1}^n 1/\varepsilon_j^2. \quad (\text{B4})$$

Defining  $H = \sum_{i=1}^n 1/\varepsilon_i^2$ , then by algebraic manipulation of (B4) the sum of the weights as a function of the normalized error variances becomes

$$n\bar{w} = \frac{H}{1 + H}. \quad (\text{B5})$$

The weights are then defined as

$$w_j = \frac{1}{(1 + H)\varepsilon_j^2}. \quad (\text{B6})$$

Using these same assumptions, the combined noise-to-signal variance ratio is

$$\varepsilon_0^2 = 1 - n\bar{w} = \frac{1}{1 + H}. \quad (\text{B7})$$

Note that these OA weights may cause damping of the solution in situations when the noise is large. To avoid this damping the weights can be normalized, giving the solution

$$q_i = \frac{1}{H\varepsilon_i^2}. \quad (\text{B8})$$

Here the sum of the normalized weights,  $q_i$ , is equal to 1. Using Kagan's Eq. (3.3.10), it can be shown that the error using normalized weights is

$$\varepsilon_q^2 = \varepsilon_0^2 + \frac{(1 - n\bar{w})^2}{n\bar{w}} = \frac{1}{H}. \quad (\text{B9})$$

Note that this error reduces to the error from (B7) as the sum of the weights approaches 1. Otherwise it is slightly larger. The normalization has been implemented in the current OI SST processing.

## REFERENCES

- Cavalieri, D. J., C. L. Parkinson, P. Gloersen, J. C. Comiso, and H. J. Zwally, 1999: Deriving long-term time series of sea ice cover from satellite passive-microwave multisensor data sets. *J. Geophys. Res.*, **104**, 15 803–15 814.
- Cayula, J.-F., and P. Cornillon, 1996: Cloud detection from a sequence of SST images. *Remote Sens. Environ.*, **55**, 80–88.
- Chelton, D. B., and F. J. Wentz, 2005: Global microwave satellite observations of sea surface temperature for numerical weather prediction and climate research. *Bull. Amer. Meteor. Soc.*, **86**, 1097–1115.
- Donlon, C. J., P. J. Minnett, C. Gentemann, T. J. Nightingale, I. J. Barton, B. Ward, and M. J. Murray, 2002: Toward improved validation of satellite sea surface skin temperature measurements for climate research. *J. Climate*, **15**, 353–369.
- Emery, W. J., D. J. Baldwin, P. Schlüssel, and R. W. Reynolds, 2001: Accuracy of in situ sea surface temperatures used to calibrate infrared satellite measurement. *J. Geophys. Res.*, **106**, 2387–2406.
- Grumbine, R. W., 1996: Automated passive microwave sea ice concentration analysis at NCEP. NOAA Tech. Note 120, 13 pp. [Available from NCEP/NWS/NOAA, 5200 Auth Road, Camp Springs, MD 20746.]
- Hock, R., and H. Jensen, 1999: Application of kriging interpolation for glacier mass balance computations. *Geogr. Ann.*, **81**, 611–619.

- Kagan, R. L., 1979: *Averaging of Meteorological Fields*. Gidrometeoizdat, 212 pp. (Translated from Russian by L. S. Gandin and T. M. Smith, Eds., Kluwer Academic, 1997.)
- Kawai, Y., H. Kawamura, S. Takahashi, K. Hosoda, H. Murakami, M. Kachi, and L. Guan, 2006: Satellite-based high-resolution global optimum interpolation sea surface temperature data. *J. Geophys. Res.*, **111**, C06016, doi:10.1029/2005JC003313.
- Kent, E. C., and P. K. Taylor, 2006: Toward estimating climatic trends in SST. Part I: Methods of measurement. *J. Atmos. Oceanic Technol.*, **23**, 464–475.
- , P. G. Challenor, and P. K. Taylor, 1999: A statistical determination of the random observational errors present in voluntary observing ships meteorological reports. *J. Atmos. Oceanic Technol.*, **16**, 905–914.
- Kilpatrick, K. A., G. P. Podesta, and R. Evans, 2001: Overview of the NOAA/NASA advanced very high resolution radiometer Pathfinder algorithm for sea surface temperature and associated matchup database. *J. Geophys. Res.*, **106**, 9179–9198.
- May, D. A., M. M. Parmeter, D. S. Olszewski, and B. D. McKenzie, 1998: Operational processing of satellite sea surface temperature retrievals at the Naval Oceanographic Office. *Bull. Amer. Meteor. Soc.*, **79**, 397–407.
- McPhaden, M. J., and Coauthors, 1998: The Tropical Ocean-Global Atmosphere (TOGA) observing system: A decade of progress. *J. Geophys. Res.*, **103**, 14 169–14 240.
- Quarty, D., and M. A. Srokosz, 2002: SST observations of the Agulhas and East Madagascar retroreflections by the TRMM Microwave Imager. *J. Phys. Oceanogr.*, **32**, 1585–1592.
- Rayner, N. A., D. E. Parker, E. B. Horton, C. K. Folland, L. V. Alexander, D. P. Rowell, E. C. Kent, and A. Kaplan, 2003: Global analyses of sea surface temperature, sea ice, and night marine air temperature since the late nineteenth century. *J. Geophys. Res.*, **108**, 4407, doi:10.1029/2002JD002670.
- Reynolds, R. W., 1993: Impact of Mount Pinatubo aerosols on satellite-derived sea surface temperatures. *J. Climate*, **6**, 768–774.
- , and T. M. Smith, 1994: Improved global sea surface temperature analyses using optimum interpolation. *J. Climate*, **7**, 929–948.
- , C. K. Folland, and D. E. Parker, 1989: Biases in satellite derived sea-surface temperature data. *Nature*, **341**, 728–731.
- , N. A. Rayner, T. M. Smith, D. C. Stokes, and W. Wang, 2002: An improved in situ and satellite SST analysis for climate. *J. Climate*, **15**, 1609–1625.
- Richman, M. B., 1986: Rotation of principal components. *J. Climatol.*, **6**, 293–335.
- Smith, T. M., and R. W. Reynolds, 2003: Extended reconstruction of global sea surface temperatures based on COADS data (1854–1997). *J. Climate*, **16**, 1495–1510.
- , and —, 2004: Improved extended reconstruction of SST. *J. Climate*, **17**, 2466–2477.
- , —, R. E. Livezey, and D. C. Stokes, 1996: Reconstruction of historical sea surface temperatures using empirical orthogonal functions. *J. Climate*, **9**, 1403–1420.
- , R. E. Livezey, and S. S. Shen, 1998: An improved method for analyzing sparse and irregularly distributed SST data on a regular grid: The tropical Pacific Ocean. *J. Climate*, **11**, 1717–1729.
- Stowe, L. L., P. A. Davis, and E. P. McClain, 1999: Scientific basis and initial evaluation of the CLAVR-1 global clear/cloud classification algorithm for the Advanced Very High Resolution Radiometer. *J. Atmos. Oceanic Technol.*, **16**, 656–681.
- Thiébaux, J., E. Rogers, W. Wang, and B. Katz, 2003: A new high-resolution blended real-time global sea surface temperature analysis. *Bull. Amer. Meteor. Soc.*, **84**, 645–656.
- Van den Dool, H. M., S. Saha, and Å. Johansson, 2000: Empirical orthogonal teleconnections. *J. Climate*, **13**, 1421–1435.
- Worley, S. J., S. D. Woodruff, R. W. Reynolds, S. J. Lubker, and N. Lott, 2005: ICOADS release 2.1 data and products. *Int. J. Climatol.*, **25**, 823–842.
- Xue, Y., T. M. Smith, and R. W. Reynolds, 2003: Interdecadal changes of 30-yr SST normals during 1871–2000. *J. Climate*, **16**, 1601–1612.